



Impacts of forest loss on local climate across the conterminous United States: Evidence from satellite time-series observations

Yang Li^{a,b,*}, Yanlan Liu^{b,c}, Gil Bohrer^{a,d}, Yongyang Cai^e, Aaron Wilson^{f,g}, Tongxi Hu^{a,b}, Zhihao Wang^h, Kaiguang Zhao^{a,b,*}

^a Environmental Science Graduate Program, The Ohio State University, Columbus, OH 43210, USA

^b School of Environment and Natural Resources, The Ohio State University, Columbus, OH 43210, USA

^c School of Earth Sciences, The Ohio State University, Columbus, OH 43210, USA

^d Department of Civil, Environmental and Geodetic Engineering, The Ohio State University, Columbus, OH 43210, USA

^e Department of Agricultural, Environmental, and Development Economics, The Ohio State University, Columbus, OH 43210, USA

^f Byrd Polar and Climate Research Center, The Ohio State University, Columbus, OH 43210, USA

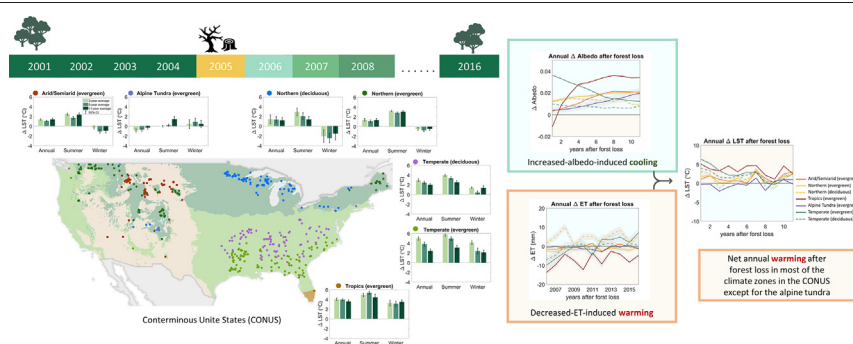
^g Department of Extension, The Ohio State University, Columbus, OH 43210, USA

^h Department of Geographical Sciences, University of Maryland, College Park, MD 20742, USA

HIGHLIGHTS

- We explore the biophysical effects of forest loss on land surface temperature.
- We use an innovative approach and the data with 30 m spatial resolution.
- Cooling of increased albedo is offset by warming of decreased evapotranspiration.
- Precipitation impacts land surface temperature by affecting evapotranspiration.
- The recovery of albedo and evapotranspiration does not necessarily synchronize.

GRAPHICAL ABSTRACT



ARTICLE INFO

Article history:

Received 16 April 2021

Received in revised form 9 August 2021

Accepted 9 August 2021

Available online 14 August 2021

Editor: Elena Paoletti

Keywords:

Forest loss

Local land surface temperature

Biophysical effects

Albedo

Evapotranspiration

ABSTRACT

Forest disturbances alter land biophysics. Their impacts on local climate and land surface temperature (LST) cannot be directly measured by comparing pre- and post-disturbance observations of the same site over time (e.g., due to confounding such as background climate fluctuations); a common remedy is to compare spatially-adjacent undisturbed sites instead. This space-for-time substitution ignores the inherent biases in vegetation between two paired sites, interannual variations, and temporal dynamics of forest recovery. Besides, there is a lack of observation-based analyses at fine spatial resolutions capable of capturing spatial heterogeneity of small-scale forest disturbances. To address these limitations, here we report new satellite analyses on local climate impacts of forest loss at 30 m resolution. Our analyses combined multiple long-term satellite products (e.g., albedo and evapotranspiration [ET]) at 700 sites across major climate zones in the conterminous United States, using time-series trend and changepoint detection methods. Our method helped isolate the biophysical changes attributed to disturbances from those attributed to climate backgrounds and natural growth. On average, forest loss increased surface albedo, decreased ET, and reduced leaf area index (LAI). Net annual warming—an increase in LST—was observed after forest loss in the arid/semiarid, northern, tropical, and temperate regions, dominated by the warming from decreased ET and attenuated by the cooling from increased albedo. The magnitude of post-disturbance warming was related to precipitation; climate zones with greater precipitation showed less warming.

* Corresponding authors at: Environmental Science Graduate Program, The Ohio State University, Columbus, OH 43210, USA.

E-mail addresses: li.10015@osu.edu (Y. Li), zhao.1423@osu.edu (K. Zhao).

stronger and longer warming. Reduction in leaf or LAI was larger in evergreen than deciduous forests, but the recovery in LAI did not always synchronize with those of albedo and ET. Overall, this study presents new evidence of biophysical effects of forest loss on LST at finer spatial resolutions; our time-series method can be further leveraged to derive local policy-relevant ecosystem climate regulation metrics or support model-based climate-biosphere studies.

© 2021 Elsevier B.V. All rights reserved.

1. Introduction

Forests provide various social-ecological services, such as climate and water regulation, biodiversity sustaining, nutrient cycling, recreation, and tourism (Alix-Garcia and Wolff, 2014; Bonan, 2008). However, forests have been in rapid decline in the past two centuries due to human activities, climate changes, and natural disturbances (e.g., wildfire, insect infestation, and hurricanes) (Allen et al., 2010; Barlow et al., 2016; Chapman et al., 2008; Hansen et al., 2013; Liu et al., 2017; Randerson et al., 2006; Senf et al., 2015). Such disturbances to forest cover and structure alter land-atmosphere interactions through biogeochemical and biophysical processes (Bright et al., 2015; Li et al., 2015; Zhao and Jackson, 2014). Loss of forests releases CO₂ to the air and impairs terrestrial biological carbon sequestration, affecting climate through intensified greenhouse effects (Gibbs and Herold, 2007; McAlpine et al., 2010; van der Werf et al., 2009). Concomitant with the modified carbon cycling from forest loss are changes in land surface biophysics that also affect energy partitioning, and impact local climate in directions that either amplify or dampen the CO₂-induced warming (Bala et al., 2007).

Forest loss affects local climate by altering the surface energy budget and water balance through changes in evapotranspiration (ET) and biophysical properties, such as albedo, surface roughness, and aerodynamic canopy conductance (Anderson et al., 2011; Eder et al., 2015; Jackson et al., 2008; Perugini et al., 2017). Such changes may contribute to large-scale atmospheric feedbacks through changes to CO₂ concentration, cloud and precipitation patterns, and changes to volatile organic compounds (VOC) and aerosol concentrations. Among a variety of factors, both data-driven and model-based studies suggest that the cooling or warming effect of deforestation is mainly driven by changes in surface albedo, ET (Bala et al., 2007; Li et al., 2015; Liu et al., 2019; Maness et al., 2013; Prevedello et al., 2019), and other biophysical mechanisms, such as surface roughness (Chen et al., 2016; Davin and de Noblet-Ducoudré, 2010; Lee et al., 2011; Winckler et al., 2017). Changes in albedo and ET that are driven by forest loss exert competing impacts on land surface temperature (LST). Enhanced albedo reduces the absorption of incoming solar radiation and thus cools the land surface (Zhao and Jackson, 2014). On the other hand, reduced leaf area leads to lower ET and latent heat flux, thereby warming the land surface (Bright et al., 2017). With deforestation, decreased surface roughness tends to reduce turbulent exchanges of heat from the surface, leading to local land-surface warming (Bonan, 2015; Chen et al., 2016; Davin and de Noblet-Ducoudré, 2010; Khanna and Medvigy, 2014; Lee et al., 2011; Winckler et al., 2017; Yuan et al., 2021). The net effect of forest loss on LST depends on the relative dominance of the cooling effect due to enhanced surface albedo and the warming effect due to decreased ET and surface roughness. Considering the internal causes for reduction in surface fluxes are indistinguishable, we assume that changes to ET represent the full surface-flux reduction effects, whether they are driven by reduced roughness, reduced leaf area, and/or changes to stomatal conductance.

The impacts of ET and albedo on LST could vary with precipitation and the recovery of the ecosystem indicated by leaf area index (LAI) (O'Halloran et al., 2012). We acknowledge that precipitation could be impacted by forest loss, and the extent of such effect on precipitation is related to the scale of deforestation (Lejeune et al., 2015; Pitman and Lorenz, 2016). Complete, large-scale deforestation could have a

stronger impact on rainfall than partial deforestation (Lawrence and Vandecar, 2015; Nobre et al., 2009). Previous studies showed significant reduction of precipitation after large-scale deforestation (Lean and Warilow, 1989; Medvigy et al., 2011; Werth and Avissar, 2002), but no correlation was found between precipitation and change of forest cover at a stand scale (de Oliveira et al., 2018; Debortoli et al., 2017). Though the impact of forest loss on precipitation may not be detectable for limited forest loss areas, the interaction between ET and LST is mediated by precipitation because of the feedback of ET on convective precipitation (Bonan, 2015; Li et al., 2020; Shen et al., 2019). The recovery rate is also subjected to biophysical or biochemical constraints and affected by the disturbance regime and climate (Anderson-Teixeira et al., 2013; Griffiths et al., 2014). A review by Anderson-Teixeira et al. (2013) pointed out that the rate of forest recovery increased with atmospheric CO₂, temperature, and precipitation. Kennedy et al. (2012) also suggested that forest recovery rate tends to be lower in ecoregions with limited moisture.

Numerous observational and model-based studies have explored how forest loss affects local, regional, and global climate via biophysical processes. Because model-based studies allow complete control over the virtual simulation environment, they can elucidate the physical mechanisms that drive observed responses by changing one variable or parameter at a time in controlled virtual experiments at scales that are impossible to control in the real world (Bonan, 2008; Laguë et al., 2019). For example, models have been used to estimate the relative strength of albedo effects relative to transpirational effects (Davin and de Noblet-Ducoudré, 2010). Model-based studies found that the relative strength of these effects varies by climatic zone, with albedo dominance in the higher latitudes and transpirational dominance in the tropics (Kvalevåg et al., 2010). Virtual experiments were used to evaluate the effects of changes to surface roughness (Banerjee et al., 2017; Burakowski et al., 2018; Khanna and Medvigy, 2014) and atmospheric feedbacks through atmospheric CO₂ concentrations and changes to precipitation patterns (Jackson et al., 2005; Laguë et al., 2019; Wang and Eltahir, 2000). Model-based studies can not only focus on processes at high resolution and small locations but also simulate in large regions, and in fact, the whole earth surface. For example, global models of virtual deforestation scenarios showed that tropical deforestation will have vast impacts on the global climate in terms of both temperature and precipitation (Bala et al., 2007; Jiang et al., 2021; Nobre et al., 2009; Shukla et al., 1990; Swann et al., 2018; Werth and Avissar, 2002). In situ measurements provided insights in local and global studies but are subjected to the inherent limitation of data availability (Bright et al., 2017).

Remote sensing complements these approaches with consistent and repeated monitoring of the land surface over a large scale and extended time period (Duveiller et al., 2018; Li et al., 2015). Studies based on satellite observations suggest that the sign and magnitude of the altered LST after forest loss vary across latitudes, revealing a warming effect at lower latitude and a cooling effect at higher latitude (Alkama and Cescatti, 2016; Duveiller et al., 2018; Li et al., 2015; Liu et al., 2019; Xu et al., 2020). Specifically, the cooling effect of enhanced albedo post-deforestation fails to offset the warming effect of drastically reduced ET in the tropics, leading to a net warming effect; whereas the cooling effect of high snow albedo in the boreal winter outpaces the warming effect of reduced growing-season ET, giving rise to net cooling. In mid-latitudes, there are contrasting reports of net warming or cooling effects

of deforestation (Li et al., 2015; Wickham et al., 2014; Zhao and Jackson, 2014). For example, Liu et al. (2019) reported net warming post fire disturbance between the latitudes of 20°N and 45°N, while Bounoua et al. (2002) suggested a local cooling after deforestation in mid-latitudes.

Most large-scale studies based on remote sensing investigate the biophysical feedbacks of deforestation at coarse spatial resolutions (e.g., 500 m or 0.05°). However, due to the high spatial heterogeneity of vegetation cover especially post-disturbance, observations at a finer resolution are necessary to capture the spatial variability of the ET and albedo, and their controls on LST. To date, most studies take space-for-time substitution as a surrogate of real land cover change (Bright et al., 2017; Duveiller et al., 2018; Li et al., 2015; Liu et al., 2019; Peng et al., 2014; Zhao and Jackson, 2014). However, the space-for-time substitution assumes that vegetations between two paired sites (i.e., disturbed site and corresponding control site) are the same, thus ignoring the spatial difference between paired sites. Besides, it assumes that current vegetation at control sites can be used as a surrogate for pre-disturbance vegetation at disturbed sites, ignoring the temporal variation because the assumption only holds when there is no interannual variation of vegetation. However, even if there is no forest loss, vegetation status varies across years due to its natural growth or due to the impact of background climate.

This study aims to further improve on the assessment of local climate impacts of forest loss based on satellite observations at fine spatial resolutions. We also address the existing limitations associated with the space-for-time substitution approach—the most prevalent method currently in use. The focus of our assessment is to provide a data-driven observation-based assessment of the direct local effects of forest loss on LST and surface energy fluxes, without fully considering large-scale feedbacks of forest loss (e.g., changes of precipitation, atmospheric CO₂ concentration, and cloud patterns). We hypothesize that a change of annual mean LST observed at a particular location that experiences forest loss is primarily driven by two opposing effects: the warming effect of decreased ET, and the cooling effect of increased albedo. A net warming will be observed where the effect of ET is stronger than the effect of albedo. This hypothesis is tested using a combination of datasets of land cover, biophysical, meteorological, and topographic conditions from remote sensing and reanalysis products across the conterminous United States (CONUS) at selected sites representing five climate zones. We specifically address the following objectives: (1) determine

the spatial and temporal variation pattern of LST due to forest loss; (2) quantify the change and recovery of surface properties (e.g., albedo and LAI) and fluxes (e.g., albedo-induced radiative forcing [RF], ET) closely related to LST after forest loss; (3) evaluate the driving effects of biophysical properties and surface fluxes on LST after forest loss.

2. Data and methods

2.1. Study area

Our study area covers the five climate zones of the CONUS (Fig. 1), as defined in the Köppen-Geiger climate classification (Beck et al., 2018). The dominant climate zones are the arid/semiarid, the temperate, and the northern (renamed from the boreal zone in the Köppen-Geiger classification to avoid ambiguity because “boreal forests” normally connotes high-latitude regions); the alpine tundra and the tropic types are less common. Our emphasis here was not on wall-to-wall continuous coverage of the whole continent, but on the analysis at local scales (i.e., a spatial resolution of 30 m), so we chose a total of 700 paired sites representing typical forest types across the five climate zones. In the selection of the sites, we also differentiated evergreen forests from deciduous forests. More specifically, for evergreen forests, we sampled 100 sites in each climate zone; for deciduous forests, we sampled 100 sites only in the temperate and northern zones because of the absence/scarcity of deciduous forest in the other three zones. The specific criteria and procedures to identify these sites will be further detailed in the next section.

2.2. Site sampling using Google earth engine

Locations of the 700 pairs of sites were determined from the combined use of topography data, the land-use/land cover data, and the forest loss data, all of which are available and processed in Google Earth Engine. Each pair of sites includes two spatially adjacent sites, one disturbed, and another intact/undisturbed. Disturbances considered here include those short-lived events with temporal forest damages and losses, with a natural recovery afterward; those permanent land cover changes (e.g., forest to urban) are excluded. To allow sufficient time to evaluate vegetation variables both prior to the disturbance and the recovery process after the disturbance, the time series in this study

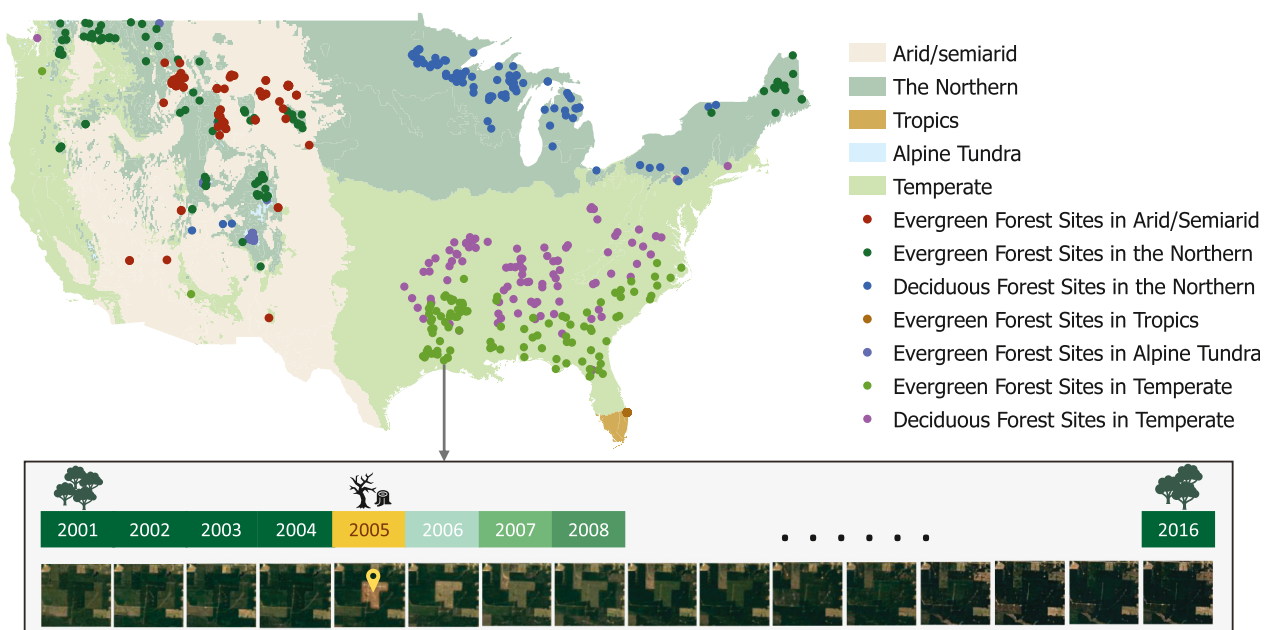


Fig. 1. Sample sites in the conterminous United States, with 100 evergreen sites in each climate zone, and 100 deciduous sites in the northern and the temperate zones. Because of the limited area of the tropics and alpine tundra, sample sites in these two regions are visually overlapped in the map, yet distinct from each other when zooming in to a finer spatial resolution.

spans from 2001 to 2016, with forest loss in 2005. To do so, we overlaid the Landsat-derived forest loss data (Hansen et al., 2013) with the USGS National Land Cover Database (NLCD), a 30 m Landsat-based land cover database covering years of 2001, 2004, 2006, 2008, 2011, 2013, and 2016, to locate the forest loss pixels in 2005. To exclude pixels that were classified as the forest clearance with no recovery hereafter, we chose the pixels with temporary forest loss rather than the pixels experiencing permanent land use or land cover change. Specifically, for all the CONUS pixels identified as “forest-loss” in 2005 based on Hansen et al. (2013), we identified those classified as “deciduous” or “evergreen” in 2001 and 2004, “non-forest” in 2006, 2008, and 2011, and the same forest type again in 2013 and 2016 based on NLCD. Each site consists of 3×3 pixels satisfying the above criterion.

Unlike the disturbed sites which experience forest loss in 2005, the control sites are categorized as forests in the NLCD continuously from 2001 to 2016. To ensure each pair of control and disturbed sites have similar climatic and edaphic conditions, we overlaid a searching window of 10 km - 30 km hollow circle on the central pixel of each disturbed site to sample the control site. Within this hollow circle, we randomly sampled 100 pixels that were categorized as forests (evergreen/deciduous) and that did not experience forest loss as candidate control sites. Only pixels with similar topographic conditions compared to disturbed sites (i.e., elevation difference less than 50 m, slope difference less than 5 degrees, and aspect difference less than 30 degrees) were retained (Liu et al., 2019). If no pixels were identified, we would expand the initial candidate pool until we found the pixel that met all requirements. Then the nearest site among all the qualified pixels was selected as the control site.

Following the above-mentioned procedures, a total number of 700 paired disturbed-control sites were selected (Fig. 1). Notably, the relatively small size of the tropical and alpine tundra regions results in concentrated sites distribution in these two climate zones. We use a temperate evergreen forest site to demonstrate the abrupt land cover change in 2005 associated with disturbance. Prior- and post-disturbance Landsat images together with manually-derived disturbed site are provided as visual references. Consistent green cover can be observed throughout 2001 to 2004 in this site, followed by disturbance in 2005 and post-disturbance recovery thereafter (Fig. 1).

2.3. Datasets

This study combines datasets of land cover, biophysical, meteorological, and topographic conditions from remote sensing and reanalysis products (Table 1). The products of the NLCD, the Hansen global forest change data, and the LST were all derived from Landsat and shared the same spatial resolution of 30 m. Landsat data was also used here to derive surface albedo. To maximize the temporal coverage of cloud-free pixels, we combined the surface reflectance from the Landsat

surface reflectance products of Landsat 5 ETM, Landsat 7 ETM+, and Landsat 8 OLI/TIRS sensors spanning from 2001 to 2016. ET and LAI products came from MODIS, with a 500 m spatial resolution. The topographic conditions were derived from the Shuttle Radar Topography Mission (SRTM) digital elevation data (Jarvis et al., 2008). Different spatial resolutions of the data products require resampling. The image-pyramid structure in Google Earth Engine allows specifying the pixel resolution of the output, thereby facilitating accessing, manipulating, and analyzing remote sensing data with on-the-fly requests (Gorelick et al., 2017; Oliphant et al., 2019; Wu et al., 2019). If the specified pixel resolution is coarser than the pixel resolution the satellite data provides, Google Earth Engine aggregates related pixels; conversely, if the specified pixel resolution is finer than the pixel resolution the satellite data provides, Google Earth Engine exports the pixel at that point. All the data except precipitation were rescaled to a 30 m resolution and exported using the Google Earth Engine; precipitation was obtained from Daymet, a 1 km \times 1 km gridded meteorological dataset interpolated from ground-station observations.

2.4. Deriving time series of LST, albedo, albedo-induced radiative forcing, ET, and LAI

2.4.1. Land surface temperature (LST)

Two types of surface temperature are often used in climatological studies: 2 m surface air temperature and LST (Jin and Dickinson, 2010). The record of 2 m surface air temperature is dependent on the distribution of meteorological stations. This gridded product is averaged with a coarse spatial resolution, and hence is often used to evaluate long-term and large-scale climate changes (Alkama and Cescatti, 2016; Hansen et al., 2006; Hooker et al., 2018). In contrast, LST is retrieved from satellite observations at relatively fine spatial and temporal resolutions, so it is often utilized to assess local or regional climate impacts (Bright et al., 2017). Besides, comparing to the 2 m air temperature, the LST is closely related to the radiative properties of the land surface (Peng et al., 2014; Zhao and Jackson, 2014; Zhou et al., 2012), as well as the interaction between albedo and ET (Li et al., 2015; Prevedello et al., 2019). Therefore, the LST is a better indicator of local surface energy partitioning. Considering that this study is based on remote sensing data and focuses on a local scale, we choose the LST to evaluate the impact of forest loss.

Many algorithms have been proposed to derive LST (Li et al., 2013; Martins et al., 2016). One of the commonly used methods is the Statistical Mono-Window (SMW) approach. The SMW approach is developed by Climate Monitoring Satellite Application Facility (CM-SAF) from the Meteosat First Generation (MFG) and the Second Generation (MSG) series of satellites. The SMW algorithm linearizes the relationship between LST and brightness temperature in the top of atmosphere (TOA) as follows:

Table 1

Datasets used to quantify biophysical changes include a range of observations of land surface characteristics and atmospheric conditions, mostly from satellites, such as land cover, surface reflectance, evapotranspiration, leaf area index, topography, and precipitation.

Dataset	Source sensor	Variable	Spatial Resolution	Reference
National Land Cover Database 2016 - Landcover & Imperviousness (NLCD2016)	Landsat	Landcover	30 m	Homer et al., 2020; Jin et al., 2019; Yang et al., 2018
Hansen Global Forest Change (v1.7)	Landsat 7 ETM+ Landsat 8 OLI/TIRS	Loss year	1 arc sec	Hansen et al., 2013
USGS Landsat 8 Surface Reflectance Tier 1	Landsat 8 OLI/TIRS	Land surface temperature, albedo:	30 m	Claverie et al., 2015; Vermote et al., 2016
USGS Landsat 7 Surface Reflectance Tier 1	Landsat 7 ETM+	surface reflectance		
USGS Landsat 5 Surface Reflectance Tier 1	Landsat 5 ETM			
MOD16A2 (v006)	MODIS Terra/Aqua	Evapotranspiration: ET_500m	500 m	Mu et al., 2011
MCD15A3H (v006)	MODIS Terra+Aqua Combined	Leaf area index: Lai_500m	500 m	Myneni et al., 2015
SRTM Digital Elevation Data (v4)		Elevation	3 arc sec	Jarvis et al., 2008
Daymet	–	Precipitation	1000 m	Thornton et al., 2017
North American Land Data Assimilation System (NLDAS) Forcing Fields	–	Shortwave radiation	0.125 arc degrees	Cosgrove et al., 2003; Luo et al., 2003

$$LST = A_i \frac{T_b}{\varepsilon} + B_i \frac{1}{\varepsilon} + C_i \quad (1)$$

where T_b and ε refer to the TOA brightness temperature and the surface emissivity of the same thermal infrared channel, respectively. A_i , B_i and C_i are the model coefficients that have been calibrated for the classes with different total column water vapor (TCWV) values and view zenith angle. This algorithm is implemented in the Google Earth Engine by [Ermida et al. \(2020\)](#). By specifying the region of interest, date range and Landsat satellite missions (Landsat 4,5,7, and 8), the LST time series of given sites can be calculated and exported. After masking the cloud, cloud shadow, and snow pixels, the LST is aggregated into monthly time series.

2.4.2. Albedo

The actual (blue-sky) shortwave albedo is calculated based on the atmospherically corrected surface reflectance from the Landsat 5 ETM sensor, the Landsat 7 ETM+ sensor and the Landsat 8 OLI/TIRS sensors spanning from 2001 to 2016. Though different Landsat sensors have slight systematic differences ([Flood, 2014; He et al., 2018](#)), it has been demonstrated that observations across the Landsat sensors can be integrated without additional bias correction ([Chen et al., 2016; Jiang et al., 2019; Qin et al., 2015](#)). During the overlapping time ranges when data from two sensors are available, the average of available surface reflectance data is used. According to [Liang \(2001\)](#), five bands are used to derive actual shortwave albedo:

$$\text{Albedo} = 0.356 \alpha_{\text{BLUE}} + 0.130 \alpha_{\text{GREEN}} + 0.373 \alpha_{\text{RED}} + 0.085 \alpha_{\text{NIR}} + 0.072 \alpha_{\text{SWIR2}} - 0.0018$$

where α_{BLUE} , α_{GREEN} , α_{RED} , α_{NIR} , α_{SWIR2} refer to the surface reflectance in blue, green, red, near-infrared, and shortwave infrared 2. Although this equation is developed using data from Landsat 4,5,7, it is still valid for Landsat 8 ([Naegeli et al., 2017; Traversa et al., 2021](#)). Clouds, cloud shadows, snow, and water pixels are masked out based on the Pixel Quality Assessment Index. The albedo of each pixel in the sampled image chips is also aggregated by averaging into monthly time series.

2.4.3. Albedo-induced radiative forcing

Albedo-induced RF is defined as the change of the reflected shortwave radiation resulting from albedo change ([Hansen et al., 1997; Vanderhoof et al., 2014](#)). It plays an essential role in predicting the LST. A simple yet effective approximation has been used by numerous studies to derive the albedo-induced RF ([Barnes and Roy, 2008; Jiao et al., 2017; Jin and Roy, 2005; Stuenzi and Schaepman-Strub, 2020; Zhang and Liang, 2014](#)).

$$RF_{\text{surf}} = -R_{\text{surf}}(\alpha_2 - \alpha_1) \quad (2)$$

where R_{surf} is the surface incoming solar radiation, α_1 and α_2 are the monthly surface albedo before and after forest loss, respectively. The incoming solar radiation is obtained from the National Land Data Assimilation System (NLDAS-2) ([Ellenburg et al., 2016](#)) and exported using Google Earth Engine.

2.4.4. Evapotranspiration (ET) and leaf area index (LAI)

ET and LAI are processed directly from MODIS products. ET describes the process whereby water is transported from the earth surface to the atmosphere by evaporation from the soil and wet vegetation, or by transpiration from plants ([Liu et al., 2020; Zhang et al., 2019](#)). The MODIS ET product (MOD16A2 V006) is derived using the Penman-Monteith equation that includes inputs of meteorological reanalysis data and remotely sensed dynamic surface properties ([Mu et al., 2011](#)). The MODIS ET product (MOD16A2 V006) and MODIS LAI product (MCD15A3H V006) provide 8-day and 4-day composite data, respectively, with 500-m pixel size. Both datasets are aggregated to monthly time series and exported using Google Earth Engine. We use quality control layers

to exclude the retrievals with poor quality caused by snow, average or high aerosol, clouds, and cloud shadow.

2.4.5. Time series reconstruction

We used the Bayesian Estimator of Abrupt change, Seasonality, and Trend (BEAST) ([Zhao et al., 2019](#)) to obtain the interannual trend under background climate in disturbed sites. Comparing to conventional single-best-model paradigms, BEAST allows flexibility to account for all the model candidates. It evaluates the probability that each model is the true model and synthesizes multiple models to derive an averaged model. Due to the nature of model-averaging, BEAST detects the change point by a continuous probability instead of a binary decision (a change point or not). This fuzzy-logic time-series algorithm helps to generate a rich set of information.

The dynamics of a long-term time series with forest loss can be decomposed into three levels: (1) the abrupt changes driven by disturbance, (2) the seasonality forced by phenological drivers, and (3) the gradual changes associated with climate background or chronic recoveries. BEAST model decomposes time-series into seasonal change, long-term trend, abrupt changes, and noise. Mathematically speaking, consider the time series of a sample pixel as $TS = \{t_i, y_i\}_{i=1, \dots, n}$, where n is the number of observations, t_i and y_i are the time i and the corresponding observation. Observation y_i can be decomposed into three components as the following equation:

$$y_i = S(t_i; \theta_S) + T(t_i; \theta_T) + \varepsilon_i \quad (3)$$

$S(t_i; \theta_S)$ and $T(t_i; \theta_T)$ indicate the seasonality and the trend, respectively. Note that the abrupt change (if exists) is implicitly embedded in the parameters θ_S and θ_T . ε_i is the residual not captured by the seasonality or the trend and is assumed to be normally distributed with a standard deviation of σ .

The reconstructed time series is the sum of the seasonality and the trend, i.e., $\hat{y}_i = S(t_i; \theta_S) + T(t_i; \theta_T)$. Here, we take a sample site in the tropics as an example. This site is in southern Florida, an area heavily damaged by Hurricane Wilma in October 2005 ([Amiro et al., 2010](#)). The time series reconstruction via the BEAST model is illustrated in [Fig. 2](#). The original time series is decomposed into the seasonality and the trend components. The probability of abrupt change is evaluated throughout the time series. Notably, an abrupt change is identified at the end of 2005 ([Fig. 2d](#)) right after Hurricane Wilma, supporting the effectiveness of the BEAST approach. We reconstructed the time series of LST, albedo, albedo-induced RF, ET, and LAI. The reconstructed gap-free time series include only the primary dynamics (seasonal change and the long-term trend) and are used in the following analysis.

Noticeably, because outliers in time series impact time series reconstruction, and further impact analyses based on the reconstructed time series, quality control is essential for all the remote sensing and reanalysis products (i.e., removing cloud, cloud shadow, and snow). Values that failed to pass quality control were masked in the time series. To ensure the credibility of reconstructed time series, we excluded monthly time series with no value for more than half a year (i.e., 6 consecutive masked values) from the reconstruction.

2.4.6. Changes in land surface variables

We used the trend detected using BEAST at each control site as the variation of land surface variables (i.e., albedo, ET, LAI, and LST) under background climate if no forest loss occurred. This trend was then subtracted from the time series at the disturbed site to isolate the impact of forest loss on land surface variables. For example, we used the BEAST model to fit an albedo time series from 2001 to 2016, including seasonal dynamics and long-term trend as in [Fig. 2\(c\)](#) and (d), respectively. Then, we calculated the detrended albedo ($TS_{\text{disturbed_detrend}}$) by subtracting the albedo trend generated at the control site ($TS_{\text{ctrl_trend}}$) from the albedo time series at the corresponding disturbed site ($TS_{\text{disturbed}}$), i.e., $TS_{\text{disturbed_detrend}} = TS_{\text{disturbed}} - TS_{\text{ctrl_trend}}$. We compared

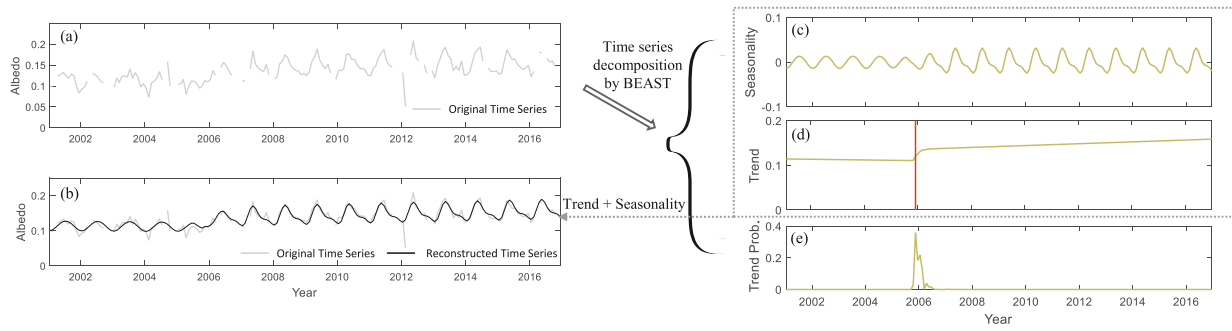


Fig. 2. An example of disturbance detection and time series reconstruction using the BEAST model. BEAST disentangles the original time series (a) into the components of seasonality (c) and the trend (d), and evaluates the probability of abrupt change along the time series (e). The red vertical bar in (d) indicates the highest probability of abrupt change at the end of 2005. The fitted time series (black line in b) is the sum of the seasonality and the trend. (For interpretation of the references to colour in this figure legend, the reader is referred to the web version of this article.)

the detrended albedo before and after forest loss to calculate the resultant albedo difference. This temporal difference of the detrended albedo (ΔAlbedo) represents the intrinsic contribution of forest loss to albedo variation. We calculated the adjusted difference of LST (ΔLST), ET (ΔET), and LAI (ΔLAI) using the same procedure (Fig. 3). The difference before and after forest loss (i.e., ΔAlbedo , ΔLST , ΔET , ΔLAI) was tested by paired t -test, and the difference among climate zones was tested by one-way ANOVA. Confidence intervals (at 95%) were also calculated for all the sites with the same climate and forest type.

2.5. Statistical analysis

We examined the relationships among ΔLST , ΔAlbedo , and ΔET . Relationships between variables are considered significant when $p < 0.001$. We also performed a stepwise regression using JMP (Matheny et al., 2014; Sall et al., 2017) to determine whether ΔAlbedo or ΔET played the most important role in predicting ΔLST

after forest loss. We started the model with an intercept-only model. The predictor that explained the most variation of ΔLST was added to the model first. After adding each predictor into this model, the overall goodness-of-fit was measured by Bayesian Information Criterion (BIC), and predictors that reduced BIC were kept in the model. All the variables were standardized by the standard deviation prior to regression. The pairwise correlation between ΔAlbedo or ΔET was also checked, and the correlation was considered significant when $p < 0.001$.

3. Results

3.1. Temporal and spatial patterns of altered LST

The temporal trend of ΔLST was heterogeneous in different climate zones. Sample sites in the arid/semiarid, the tropical, the temperate (both deciduous and evergreen forests), and the northern (both deciduous and evergreen forests) generally became warmer after forest loss

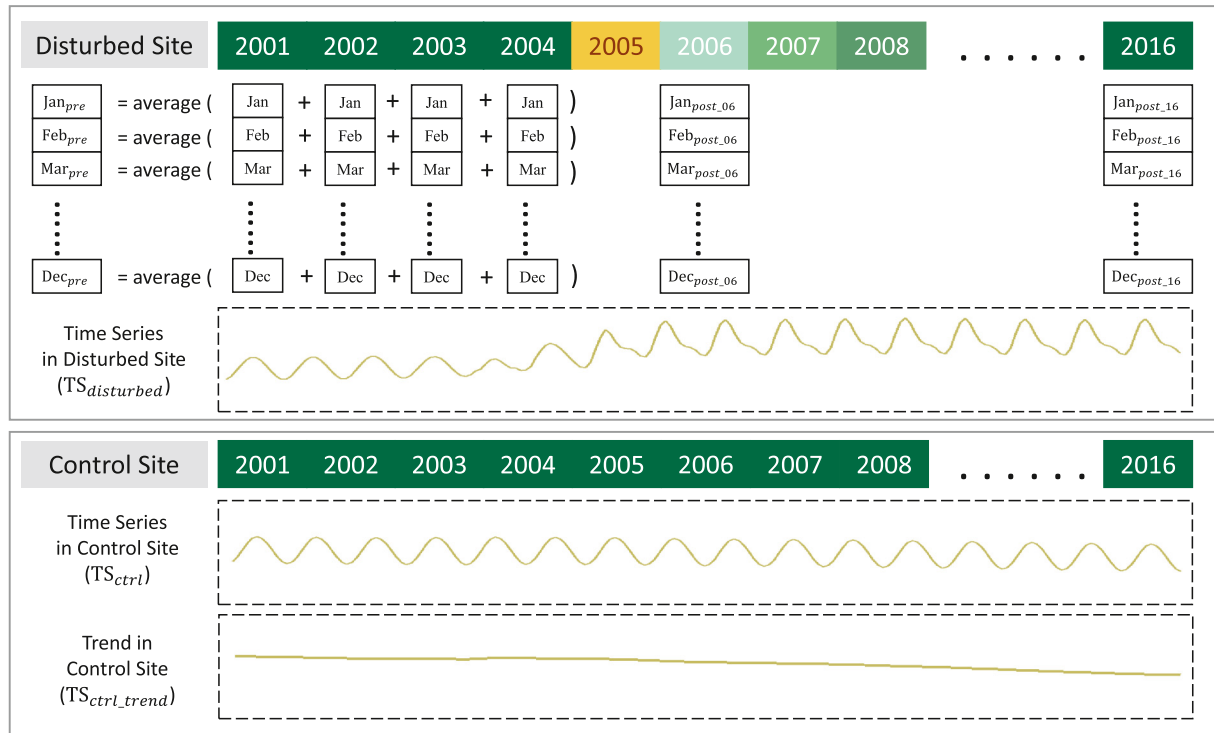


Fig. 3. The derivation of change induced by forest loss. $TS_{\text{disturbed}}$, TS_{ctrl} and $TS_{\text{ctrl_trend}}$ refer to the time series at a disturbed site, a control site, and the trend of time series at a control site, respectively. The detrended time series at the disturbed site ($TS_{\text{disturbed_detrend}}$) is derived by subtracting $TS_{\text{ctrl_trend}}$ from $TS_{\text{disturbed}}$. Pre-disturbance monthly mean (e.g. Jan_{pre}) is calculated by averaging the data at the same month before forest loss in $TS_{\text{disturbed_detrend}}$. Then the monthly land surface variable change in each year (e.g. $Jan_{\text{post_06}}$) is calculated by subtracting the pre-disturbance monthly mean from the current month in $TS_{\text{disturbed_detrend}}$.

(Fig. 4). The 11-year annual average Δ LST across the categories was 1.39 ± 0.28 °C, 3.56 ± 0.33 °C, 1.98 ± 0.27 °C, 2.41 ± 0.45 °C, 1.17 ± 0.66 °C and 1.27 ± 0.35 °C, respectively (Fig. 5). The sample sites in alpine tundra were slightly cooler with an 11-year annual mean Δ LST of -0.31 ± 0.35 °C (Fig. 5). On a seasonal scale, forest loss led to warming in both summer and winter in the tropical and temperate zones, making the annual warming effect the most prominent in these two climate zones. In arid/semiarid and northern forests, consistent summer warming was attenuated by winter cooling after the disturbance; however, the winter cooling was dwarfed by the summer warming, leading to overall annual warming in these sites. A different pattern was observed in the alpine tundra, where slight summer warming was accompanied by strong winter cooling, leading to an annual cooling effect in most of the years.

Multi-year averaged Δ LST could reflect how the LST changed along with the recovery of forest (Fig. 5). In the temperate evergreen and deciduous forests, multi-year averaged annual Δ LST after forest loss continuously decreased, suggesting that the warming effect decreased with forest recovery. Nonetheless, the warming effect decreased much slower in temperate deciduous forests compared to the trend in temperate evergreen forests (Fig. 5). In the alpine tundra, multi-year averaged annual Δ LST after forest loss increased with forest recovery, suggesting the cooling effect declined with forest recovery (Fig. 5). However, the changes in the arid/semiarid evergreen, tropical evergreen, northern evergreen and northern deciduous were statistically insignificant because the uncertainty ranges of the 3-, 5-, and 11-year averages largely overlapped with each other.

3.2. Temporal and spatial patterns of altered albedo and albedo-induced RF

3.2.1. Albedo

Forest loss generally resulted in increased albedo (Fig. 6) due to more exposed understory plants or bare soil after forest loss. One exception was the tropical zone, where annual Δ Albedo in the first year after forest loss was negative, likely caused by the exposure of darker underlying surfaces with greater soil moisture after disturbance in the sample sites (O'Halloran et al., 2012). Though Δ Albedo was mostly positive right after forest loss, the trend of Δ Albedo during the recovery differed across climate zones (Fig. 6). The albedo in the arid/semiarid and tropical evergreen forests continuously deviated from its pre-disturbance status until 2013 and then plateaued. The albedo in the alpine tundra and northern evergreen forests monotonically increased, indicating an even longer recovery time to reach the pre-disturbance state. In the temperate zone, albedo started to recover right after forest loss, suggesting a shorter recovery time of albedo. Compared to the evergreen forests in the northern and temperate zones, the deciduous forests showed lower Δ Albedo with less interannual variation (Fig. 6).

Unlike annual Δ Albedo, seasonal Δ Albedo specifies the responses in the summer and in the winter. As shown in Fig. 7, forest loss exerted a

significantly greater impact on albedo in the summer than in the winter for all the climate zones except for the tropics, where the 11-year averaged Δ Albedo was similar between the summer ($29.00 \pm 0.50 (\times 10^{-3})$) and the winter ($28.00 \pm 0.53 (\times 10^{-3})$). Unlike tropical evergreen forests, the seasonality of tree canopy was stronger in other climate zones due to phenology. Noticeably, the annual variation amplitude of albedo in tropical evergreen forests was significantly lower than those in all other climate zones (Table A1). A large seasonal amplitude of albedo indicated a much darker surface in the summer than in the winter likely due to canopy phenology. Therefore, the impact of the forest loss on albedo was similar throughout the year in tropical evergreen forests but more prominent in the summer than in the winter in other climate zones. For instance, in the arid/semiarid zone, the 11-year averaged Δ Albedo was $19.53 \pm 0.61 (\times 10^{-3})$ in the summer, but only $13.45 \pm 0.39 (\times 10^{-3})$ in the winter (Fig. 7). The same pattern was also identified in the northern, alpine tundra, and temperate zones.

3.2.2. Albedo-induced RF

The altered surface albedo induces shortwave surface RF. RF is defined as the perturbation to the radiation balance of the climate system (Zhao and Jackson, 2014). Due to increased albedo after forest loss, the albedo-induced RF was negative (i.e., less net radiation) in all the five climate zones (Fig. 8). The increasing trend of RF after deforestation in the temperate evergreen zone was opposite to the decreasing trend in the other four climate zones (Figs. 8, 9), which was consistent with the trends of Δ Albedo (Fig. 6). The RF in the deciduous forests was less variable compared to the RF in the evergreen forests within the same climate zone, which also aligned well with the pattern observed from Δ Albedo (Fig. 6). Compared to the RF in the summer, the RF in the winter was less variable in all the climate zones except for the tropical and temperate evergreen (Figs. 8b, c, 9). The relatively stable RF in the arid/semiarid, the northern, and the alpine tundra could be attributed to similar canopy cover in the winter before and after forest loss.

3.3. Temporal and spatial patterns of altered ET

Annual Δ ET gradually recovered in all the climate zones except for the alpine tundra, where ET deviated further from the pre-disturbance state (Fig. 11). In most climate zones, the Δ ET averaged across 3 years, 5 years and 11 years after forest loss progressively became less negative (Fig. 11), but the recovery pattern in each climate zones differed (Fig. 10). The tropical evergreen had continuously negative annual Δ ET after forest loss, with the 11-year averaged annual Δ ET of -7.23 ± 0.48 mm. In contrast, ET of the temperate evergreen and deciduous forests reduced in the first 3 years after forest loss (i.e., averaged annual Δ ET equaled to -6.51 ± 0.34 mm and -3.81 ± 0.37 mm, respectively), and then recovered back to pre-disturbance condition, with the 11-year

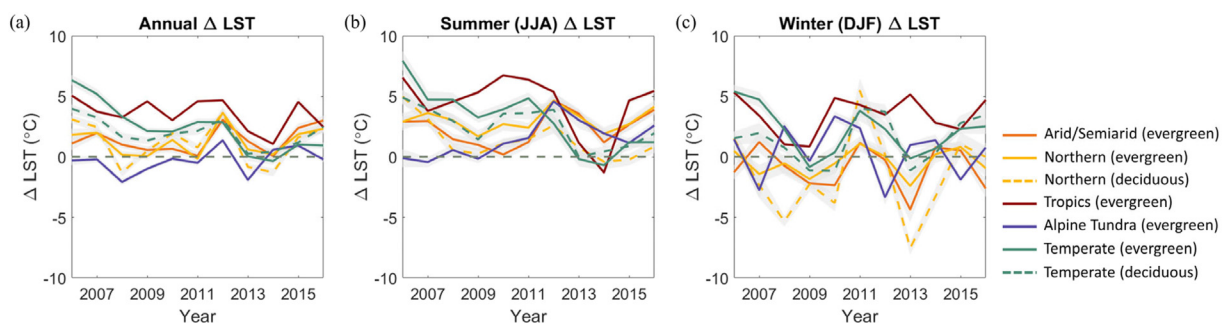


Fig. 4. Temporal variation of averaged altered land surface temperature (Δ LST) annually (a), in summer (b), and in winter (c) after forest loss. Positive Δ LST suggests warming effect, and vice versa. Grey shaded area denotes the 95% confidence interval for all the sites with the same climate and forest type. Both annual and seasonal Δ LST differ significantly across climate zones. Annual and Summer Δ LST are significant right after the forest loss in all the regions except for the alpine tundra. Winter Δ LST is not significant in northern evergreen in most of the years.

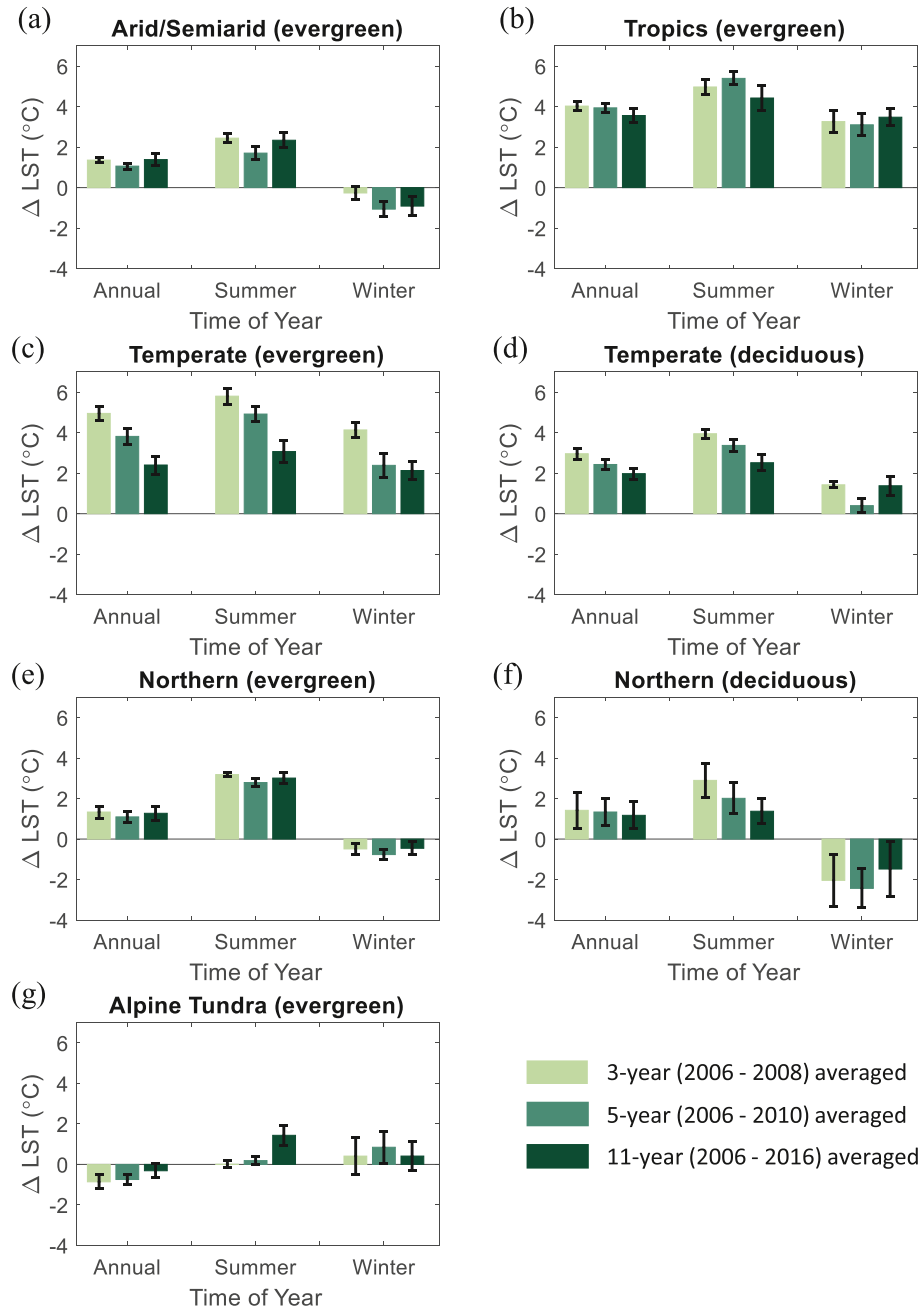


Fig. 5. Annual, summer, and winter altered land surface temperature (ΔLST) averaged 3-year, 5-year, and 11-year post forest loss in different climate zones. The 3-year averaged ΔLST reflects the LST change right after forest loss, while 5-year and 11-year averaged ΔLST represent the combined effects of forest loss and recovery on local LST. Error bars represent 95% confidence interval.

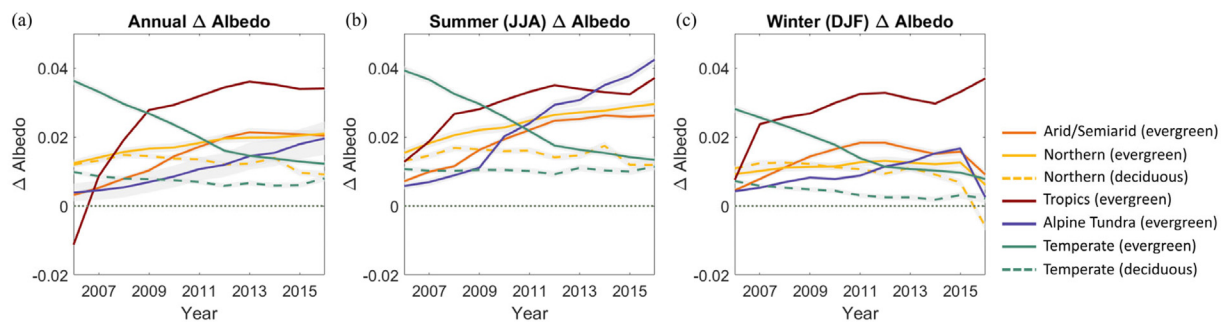


Fig. 6. Temporal variation of averaged $\Delta Albedo$ annually (a), in summer (b), and in winter (c) after forest loss. Positive $\Delta Albedo$ suggests enhanced albedo, and vice versa. Grey shaded area denotes the 95% confidence interval for all the sites with the same climate and forest type. Both annual and seasonal $\Delta Albedo$ differ significantly across climate zones. With a few exceptions, annual and seasonal $\Delta Albedo$ are significantly different from zero in all the climate zones.

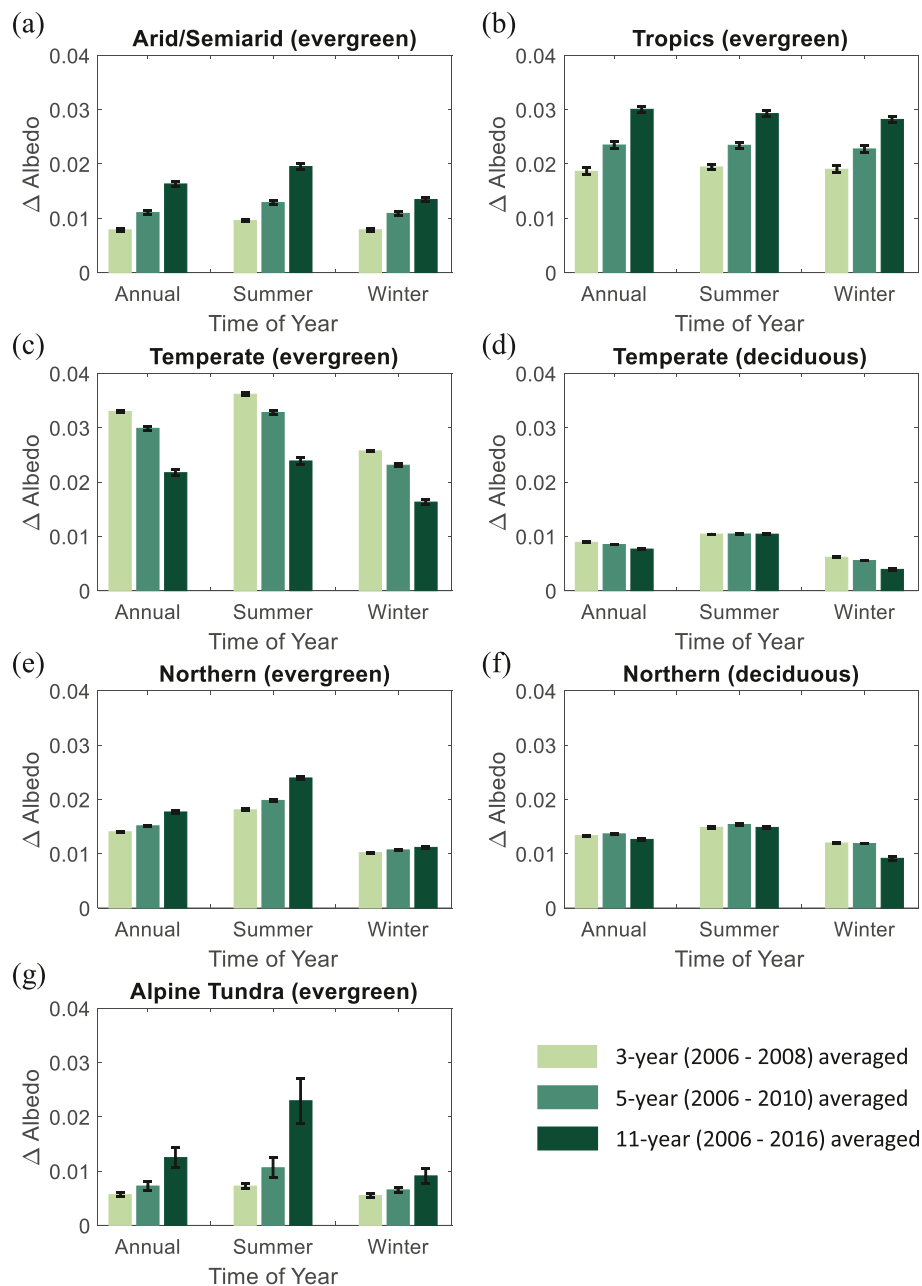


Fig. 7. Annual, summer, and winter Δ Albedo averaged 3-year, 5-year, and 11-year post forest loss in different climate zones. The 3-year averaged Δ Albedo reflects the albedo change right after forest loss, while 5-year and 11-year averaged Δ Albedo represent the combined effects of forest loss and recovery on albedo. Error bars represent 95% confidence interval.

averaged annual Δ ET of -0.27 ± 0.52 mm and -0.68 ± 0.28 mm, respectively. ET of evergreen forests in the arid/semiarid, northern, and alpine tundra regions were less impacted by forest loss. Over the 11 years post-disturbance, ET in these zones showed no clear trend and the average change was -0.47 ± 0.12 mm, -1.47 ± 0.10 mm, and -0.79 ± 0.10 mm, respectively. The impact of the forest loss on ET was stronger in the summer than in the winter (Fig. 10b, c). Noticeably, winter Δ ET in the arid/semiarid, northern, alpine tundra, and temperate regions was close to 0. This is due to the similar canopy cover during the winter before and after forest loss, and due to the fact that low winter temperature leads to low actual ET, which makes any changes in winter ET appear to be small. However, forest loss led to an apparent reduction in the winter ET in the tropical region because canopy cover reduced after disturbance all-year round, including the winter season, and because of higher actual ET during tropical winter compared to other climate zones.

3.4. Temporal and spatial pattern of altered LAI

Albedo did not recover to the pre-disturbance state even 11 years after the forest loss (Fig. 7), but ET largely recovered in most climate zones (Fig. 11). To understand the opposite patterns of albedo and ET, we also examined the recovery of canopy cover as reflected by LAI. From Fig. 12, forest loss resulted in decreased LAI in all the climate zones, with a stronger impact on the evergreen forests than on the deciduous forests. Specifically, the 11-year averaged annual Δ LAI in the northern and temperate evergreen forests was -0.198 ± 0.010 m²/m² and -0.184 ± 0.022 m²/m², respectively; whereas the 11-year averaged annual Δ LAI in the northern and temperate deciduous forests was -0.015 ± 0.003 m²/m² and -0.037 ± 0.009 m²/m², respectively (Fig. 13). The recovery pattern of LAI in evergreen forests also differed across the climate zones. Annual Δ LAI progressively became more negative in the arid/semiarid and the alpine tundra, decreasing from the

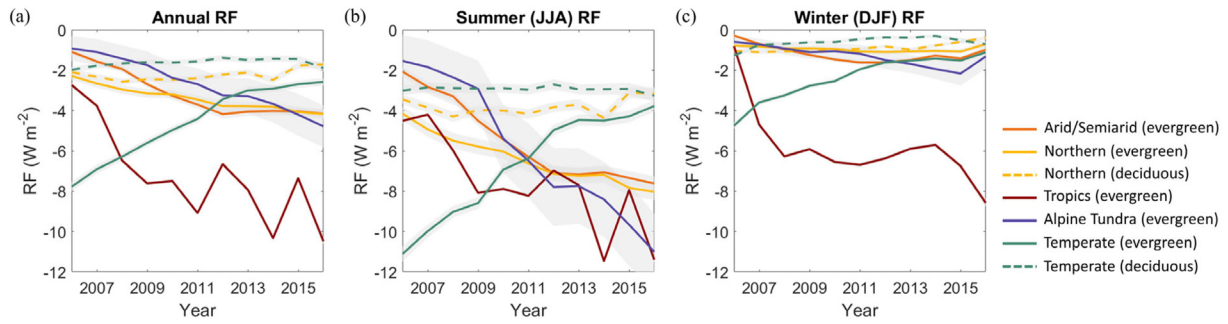


Fig. 8. Temporal variation of averaged albedo-induced radiative forcing (RF) annually (a), in summer (b), and in winter (c) after forest loss. Positive RF indicates increased radiative energy flux, and vice versa. Grey shaded area denotes the 95% confidence interval for all the sites with the same climate and forest type. Both annual and seasonal RF differ significantly across climate zones.

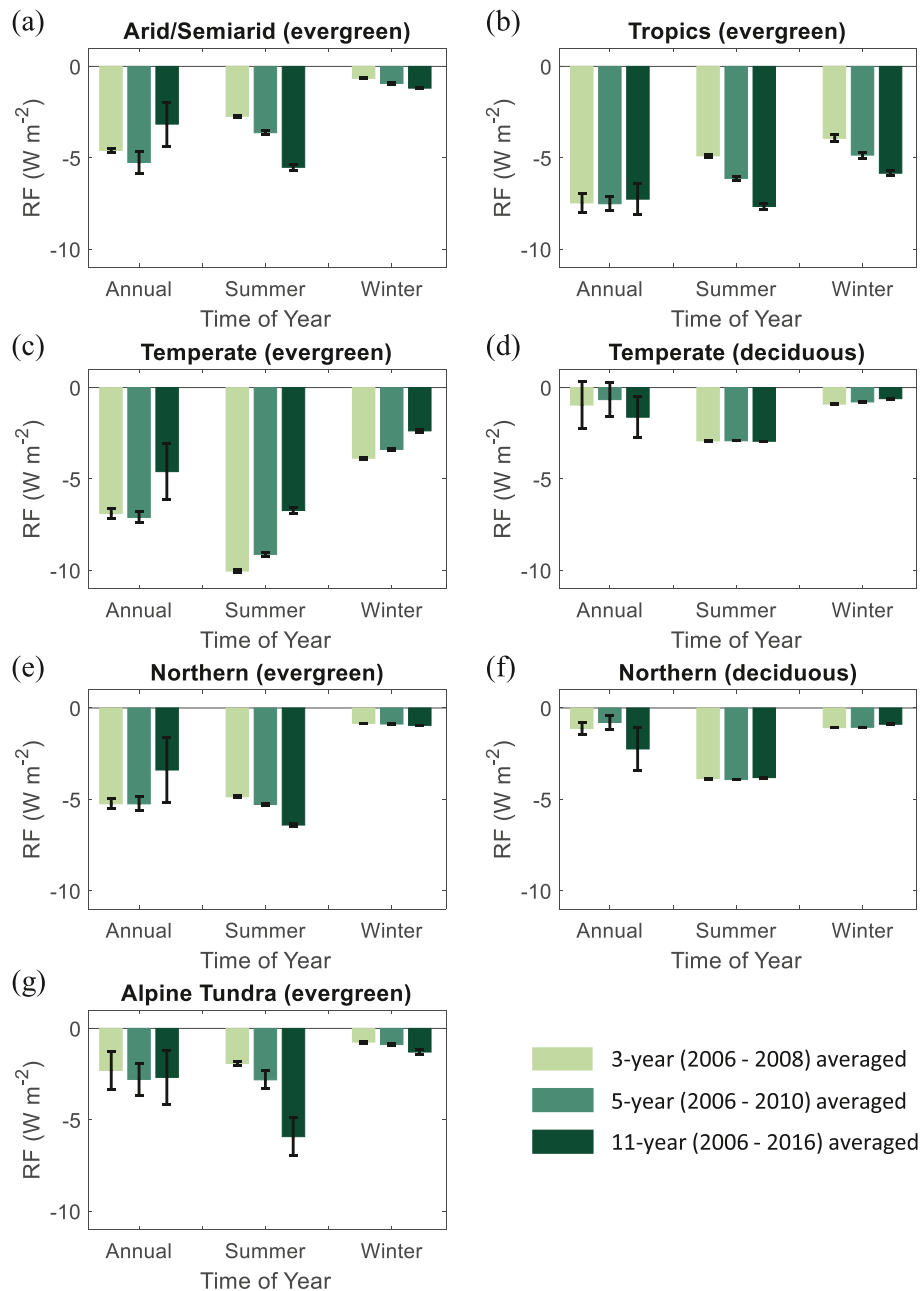


Fig. 9. Annual, summer, and winter albedo-induced radiative forcing (RF) averaged 3-year, 5-year, and 11-year post forest loss in different climate zones. The 3-year averaged RF reflects the radiative energy change right after forest loss, while 5-year and 11-year averaged RF represent the combined effects of forest loss and recovery on radiative energy flux. Error bars represents 95% confidence interval.

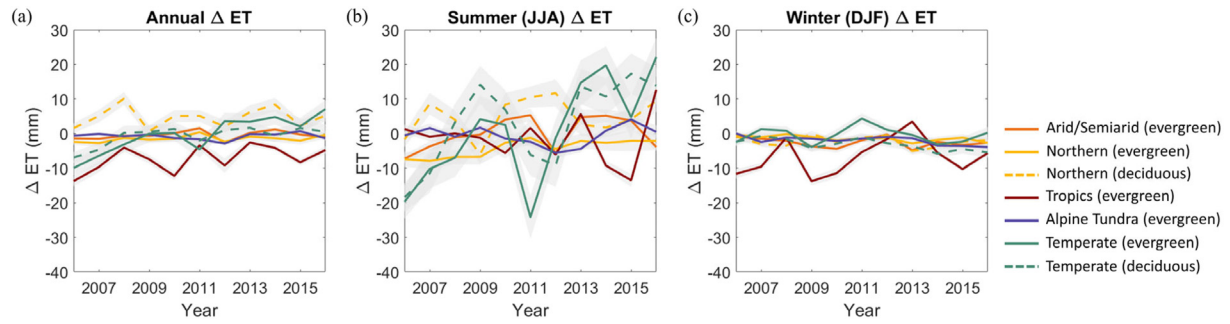


Fig. 10. Temporal variation of averaged altered evapotranspiration (ΔET) annually (a), in summer (b), and in winter (c) after forest loss. Positive ΔET suggests increased ET, and vice versa. Grey shaded area denotes the 95% confidence interval for all the sites with the same climate and forest type. Both annual and seasonal ΔET differ significantly across climate zones. Annual ΔET is significantly different from zero right after forest loss in all the regions except for the northern deciduous forests. Summer ΔET is not significant right after forest loss in northern deciduous, and evergreen in the tropics and alpine tundra. Winter ΔET is not significant in northern forests for most of the years.

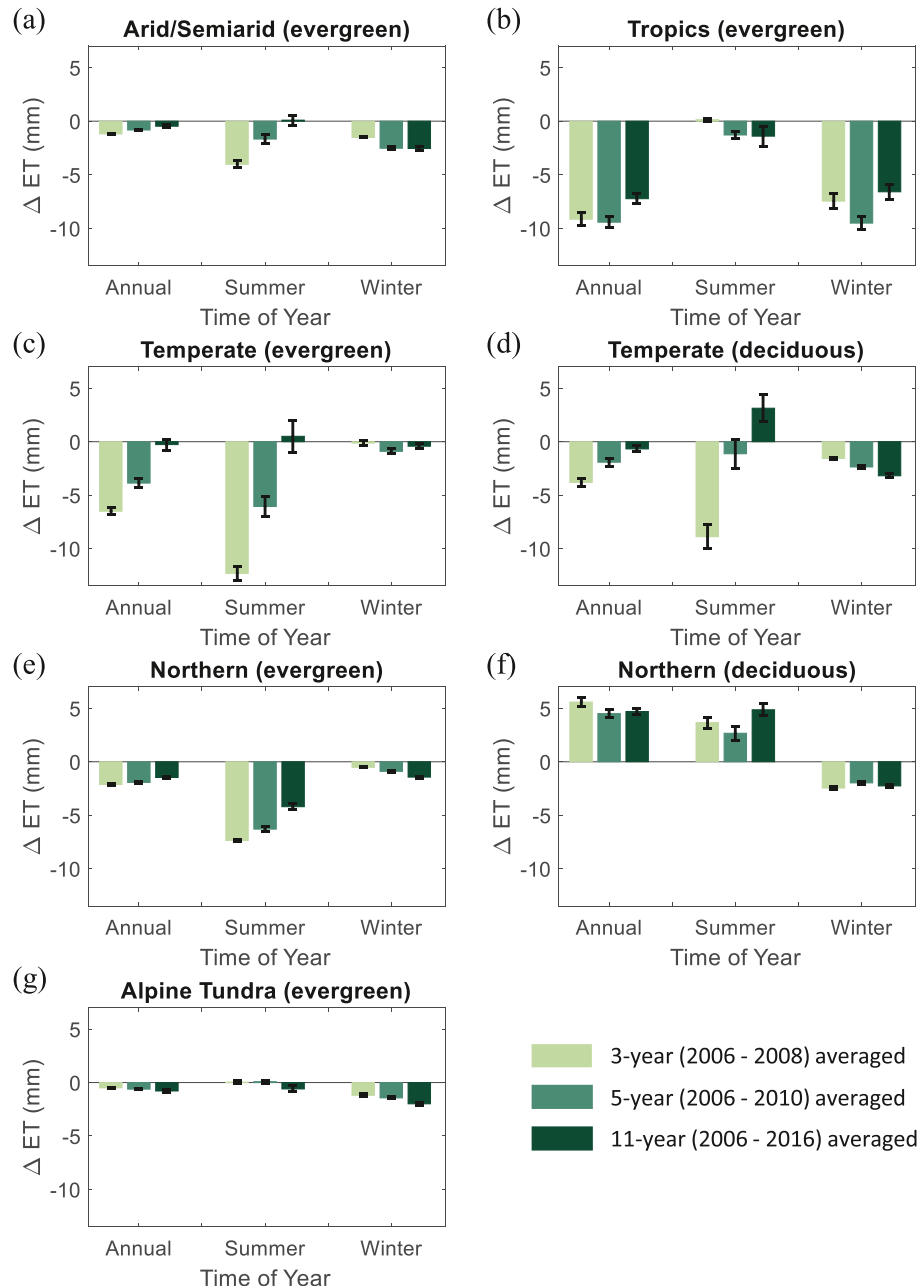


Fig. 11. Annual, summer, and winter altered evapotranspiration (ΔET) averaged 3-year, 5-year, and 11-year post forest loss in different climate zones. The 3-year averaged ΔET reflects the ET change right after forest loss, while 5-year and 11-year averaged ΔET represent the combined effects of forest loss and recovery on ET. Error bars represent 95% confidence interval.

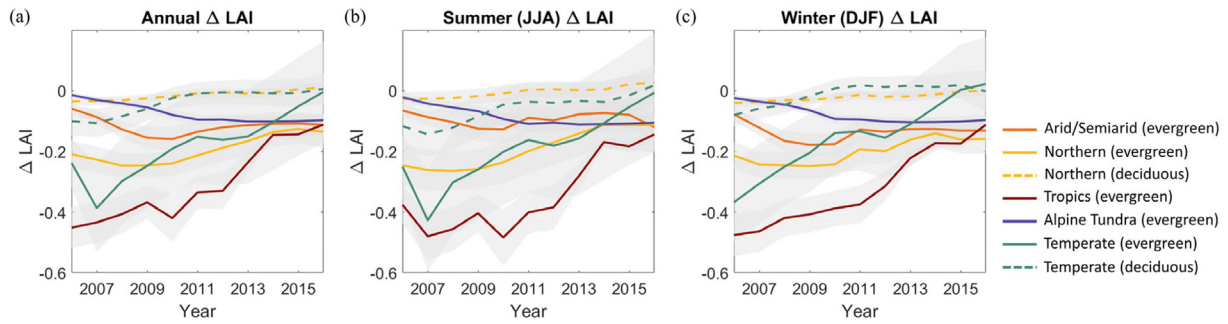


Fig. 12. Temporal variation of averaged altered leaf area index (Δ LAI) annually (a), in summer (b), and in winter (c) after forest loss. Negative Δ LAI suggests the loss of leaf area. Increased Δ LAI trend indicates the recovery of forests in disturbed sites, and vice versa. Grey shaded area denotes the 95% confidence interval for all the sites with the same climate and forest type. Both annual and seasonal Δ LAI differ significantly across climate zones. Annual and seasonal Δ LAI are significantly different from 0 right after the forest loss in all the climate zones except for the summer Δ LAI in northern deciduous forest. Δ LAI of the temperate evergreen, as well as the northern and temperate deciduous forests shifts from significant to not significant with the recovery of forests.

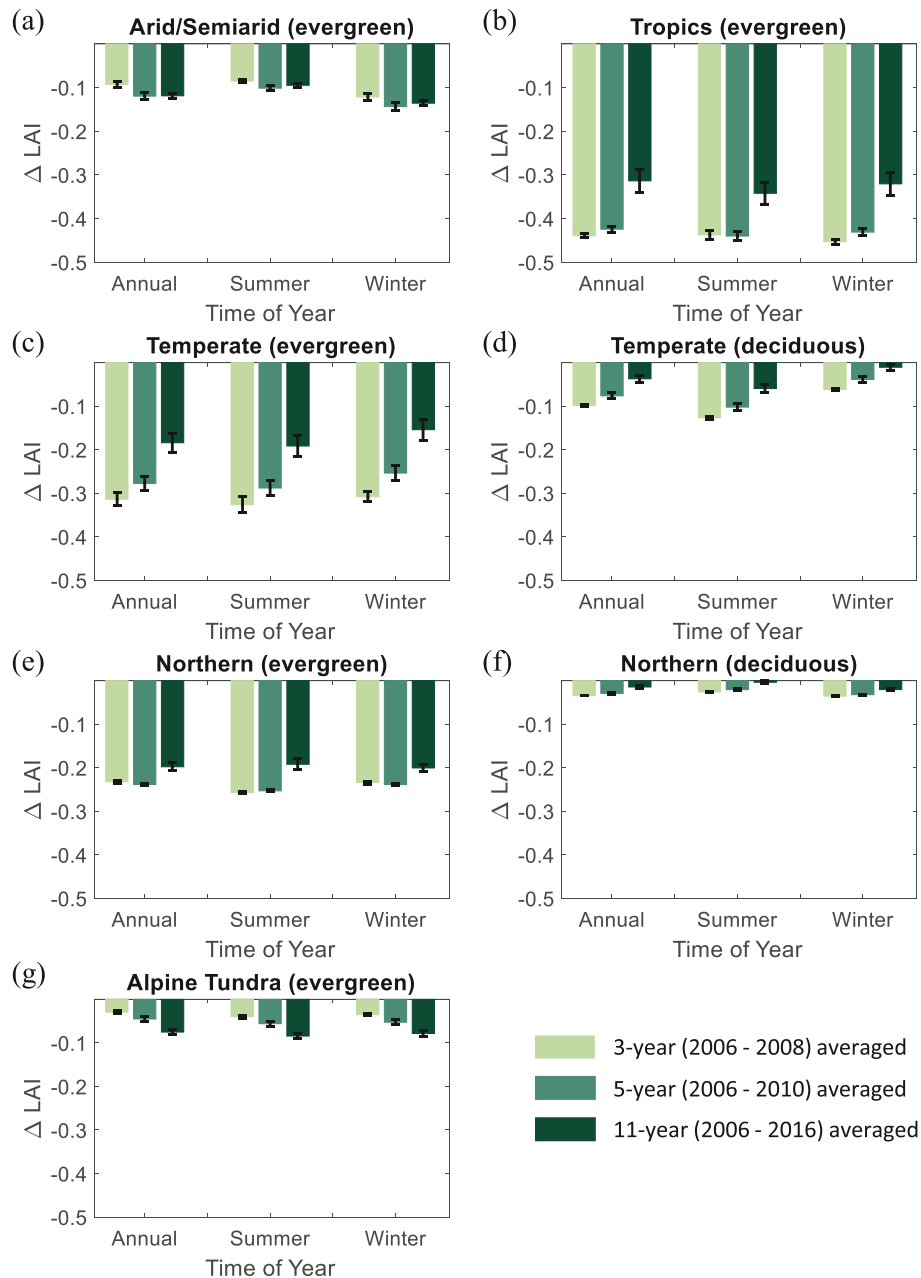


Fig. 13. Annual, summer, and winter altered leaf area index (Δ LAI) averaged 3-year, 5-year, and 11-year post forest loss in different climate zones. The 3-year averaged Δ LAI reflects the LAI change right after forest loss, while 5-year and 11-year averaged Δ LAI measure the combined effects of forest loss and recovery on LAI. Error bars represents 95% confidence interval.

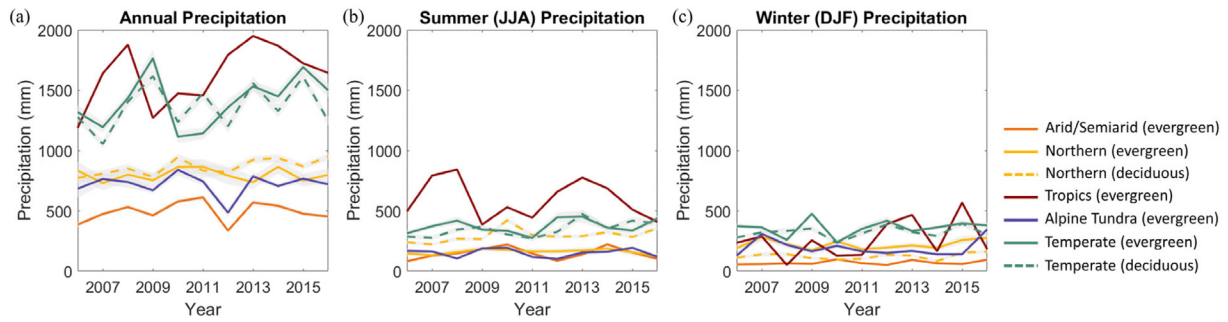


Fig. 14. Temporal variation of post-disturbance annual precipitation (a), summer precipitation (b), and winter precipitation (c). Grey shaded area denotes the 95% confidence interval for all the sites with the same climate and forest type. Both annual and seasonal precipitation differ significantly across climate zones.

3-year average of $-0.093 \pm 0.007 \text{ m}^2/\text{m}^2$ to the 11-year average of $-0.119 \pm 0.006 \text{ m}^2/\text{m}^2$ in the arid/semi-arid, and from $-0.029 \pm 0.003 \text{ m}^2/\text{m}^2$ to $-0.075 \pm 0.007 \text{ m}^2/\text{m}^2$ in the alpine tundra. A possible explanation is that the disturbance type in these two regions is mainly beetle infestation (Fig. A1). Beetle infestation leads to a gradual decrease in LAI rather than a sharp drop, because in beetle-infested forests, snags begin to fall off five years after stand death and this process peaks after ten to fifteen years (Mitchell and Preisler, 1998; Vanderhoof et al., 2014). In contrast, the annual ΔLAI in other climate zones became less negative as the forest recovered, especially in the temperate and tropical evergreen, where the annual ΔLAI increased from $-0.314 \pm 0.015 \text{ m}^2/\text{m}^2$ to $-0.184 \pm 0.022 \text{ m}^2/\text{m}^2$, and from $-0.440 \pm 0.005 \text{ m}^2/\text{m}^2$ to $-0.314 \pm 0.026 \text{ m}^2/\text{m}^2$, respectively.

3.5. Temporal and spatial pattern of precipitation

As expected, precipitation differed across climate zones. The annual precipitation in the tropical and temperate regions exceeded 1000 mm, while the arid/semi-arid, northern, and alpine tundra regions received less annual precipitation (Fig. 14). Precipitation in the northern, alpine tundra, and temperate

regions were similar in the summer and in the winter, in contrast to large seasonal variations in the tropics. In the summer, the tropics received the most precipitation compared to other climate zones but had less precipitation compared to the temperate region during the winter.

3.6. Response of ΔLST to ΔAlbedo and ΔET in evergreen forests

In this study, evergreen forest dataset is available in all the climate zones, whereas deciduous forest is limited to the temperate and northern regions. Therefore, to explore how the changes of albedo and ET are related to altered LST after forest loss, we focus on evergreen forests in all the climate zones.

3.6.1. Relationships between ΔAlbedo and ΔLST

Fig. 15(a–c) illustrates the relationship between ΔAlbedo and ΔLST . Positive ΔAlbedo after forest loss was associated with increased ΔLST . As a result of increased albedo, more negative RF (i.e., less absorbed incoming solar radiation) after forest loss also corresponded to higher ΔLST (Fig. 15d–f), suggesting that the impacts of albedo-induced RF on ΔLST was offset by non-radiative mechanisms, such as the reduced

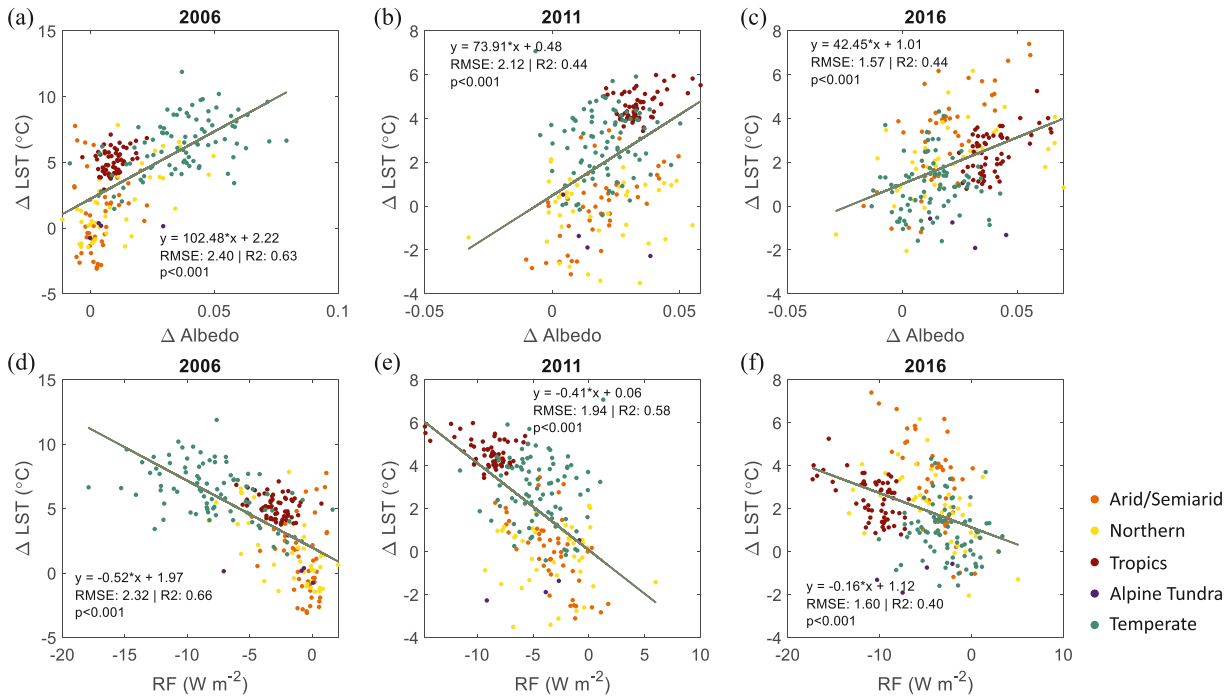


Fig. 15. Fitting annual land surface temperature change (ΔLST) with annual ΔAlbedo (a–c) and radiative forcing (RF) (d–f), respectively, in 2006, 2011, and 2016. The dots with different colors refer to sampled evergreen pixels in different climate zones. The grey line represents the relationship between ΔLST and ΔAlbedo (a–c) and RF (d–f), respectively. The trend of the grey line suggests how ΔAlbedo (a–c) and RF (d–f) are related to ΔLST , respectively. R^2 denotes how much variation in ΔLST has been explained by each predictor. Pixels with insufficient observations are masked out (as we described in Section 2.4.5).

ET of forest loss. Over the 11 years following forest loss, Δ Albedo explained 44%–63% of the Δ LST variation across sites and climate zones.

3.6.2. Relationship between Δ ET and Δ LST

From 2006 to 2016, the majority of Δ ET shifted from negative to near zero or even positive, indicating recovery of plant water use after disturbance (Fig. 16). Besides, the increase of Δ ET was related to the decrease of Δ LST; though the response sensitivities differed across climate zones, the pattern remained consistent (Fig. A2). This supports the cooling effect of ET. Δ ET explained 25%–53% of the variation of Δ LST across sites and climate zones, less than the R^2 between Δ Albedo and Δ LST.

3.6.3. Stepwise fit for Δ LST

The stepwise fit for Δ LST was performed based on the data spanning from 2006 to 2016. Annually averaged Δ Albedo and Δ ET were used as predictors. The model that includes both predictors is preferred over a simple linear regression model because BIC continuously decreases in the second step. The results of the stepwise fit suggest that both Δ Albedo and Δ ET are significant in fitting Δ LST, but Δ Albedo plays a more important role than Δ ET in predicting Δ LST after the forest loss. The statistical interpretation of the relative importance of Δ Albedo and Δ ET in fitting post-disturbance Δ LST should be taken carefully as we will discuss in Section 4.3. The estimated slope of Δ Albedo was positive, aligning well with the pattern in Fig. 15(a–c). For Δ ET, the negative slope was also in agreement with the trend in Fig. 16. Δ Albedo and Δ ET explain less variation of Δ LST compared to Fig. 15(a–c) and 16, respectively. Because we use the data spanning from 2006 to 2016 in the stepwise fit for Δ LST, this 11-year period after disturbance includes the variation resulting from forest recovery.

4. Discussion

4.1. Impacts of forest loss on albedo and ET

Both annual and seasonal albedo increased in all the five climate zones after forest loss (Fig. 6). Albedo in the temperate evergreen and deciduous forests progressively recovered back to the pre-disturbance status. However, albedo in all other climate zones deviated from the original condition, especially in the tropics where the annual Δ Albedo drastically increased from -0.01 in 2006 to 0.036 in 2016 (Fig. 6). The consistently increasing Δ Albedo was not attributed to further deterioration of vegetation after initial disturbance or further forest loss by human activities, because the sampling procedure ensured that the sampled pixels only experienced forest loss in 2005 and gradually recovered thereafter (as described in Section 2.2). However, we realize that even with such a filtering procedure, sites that recovered back to the same forest type may have shifted canopy structure and species composition, possibly making the albedo diverged from that prior to disturbance. In addition, further exposure of the soil surface has been

observed after beetle infestation and wildfires (Landry et al., 2016; O'Halloran et al., 2012; Russell et al., 2006; Vanderhoof et al., 2013). Beetle infestations gradually decrease leaf and snags in forests after stand death, resulting in a gradually increased exposure to snow in winter, thereby increasing the albedo (Landry et al., 2016; O'Halloran et al., 2012; Vanderhoof et al., 2013). Albedo after wildfires may also continue to increase because the dead snags after burning gradually fall off, resulting in a gradual increase of exposed land surface (Goetz et al., 2007; O'Halloran et al., 2012; Randerson et al., 2006), especially when half of dead snags have been reported fallen after 5–15 years postfire (Russell et al., 2006).

Unlike albedo that increased in all climate zones after forest loss, we found local ET did not necessarily decrease after forest loss. Specifically, compared to the tropical and temperate zones, Δ ET in the northern deciduous forests was positive immediately after the forest loss (Fig. 10, 11). This finding contradicted some existing studies that revealed decreased ET after wildfires (Bond-Lamberty et al., 2009; Kang et al., 2006; Ma et al., 2020; Poon and Kinoshita, 2018), typhoon (Hirano et al., 2017), and mountain pine beetles (Hubbard et al., 2013; Maness et al., 2013; Mikkelsen et al., 2013). However, one mechanism revealed by previous studies showed that decreased transpiration could be offset by increased ET from understories or forest floors (Mikkelsen et al., 2013; Nolan et al., 2015); another mechanism suggested that annual ET decreased with the age of forests (Delzon and Loustau, 2005; Lane and Mackay, 2001; Moran and O'Shaughnessy, 1984; Roberts et al., 2001; Vertessy et al., 2001). Both mechanisms support post-disturbance increases in local ET.

We expect that Δ Albedo and Δ ET converge to zero along with the recovery of forests. For instance, with the recovery of the annual LAI in the temperate evergreen (Fig. 12), the annual Δ Albedo decreased from the 3-year annual average of $33.01 \pm 0.45 (\times 10^{-3})$ to the 11-year annual average of $21.72 \pm 1.16 (\times 10^{-3})$ (Fig. 7), and the annual Δ ET increased from -6.51 ± 0.68 mm to -0.27 ± 1.05 mm accordingly (Fig. 11). Similarly, as the annual Δ LAI in the alpine tundra sites continuously decreased from 2006 to 2016 (Fig. 12), the Δ Albedo increased from the 3-year annual average of 5.65 ± 0.76 to the 11-year annual average of 12.49 ± 3.68 (Fig. 7), while the Δ ET decreased from -0.50 ± 0.07 mm to -0.79 ± 0.19 mm (Fig. 11). However, the recovery pattern of albedo did not synchronize with the recovery pattern of ET in the tropical and the northern evergreen forests. Specifically, the annual Δ LAI in the tropical and the northern evergreen regions continuously increased after forest loss (Fig. 12), corresponding well with the Δ ET trend (Fig. 11) but contradicted the increased pattern of the Δ Albedo (Fig. 7). The fact that the annual ET in the tropical and the northern evergreen areas gradually recovered to its initial status implied the gradual recovery of forest from the perspective of water use. However, the annual Δ Albedo in those two regions kept deviating from the original status after forest loss, suggesting that the secondary succession of forests at the disturbed sites did not force the albedo back to the initial state.

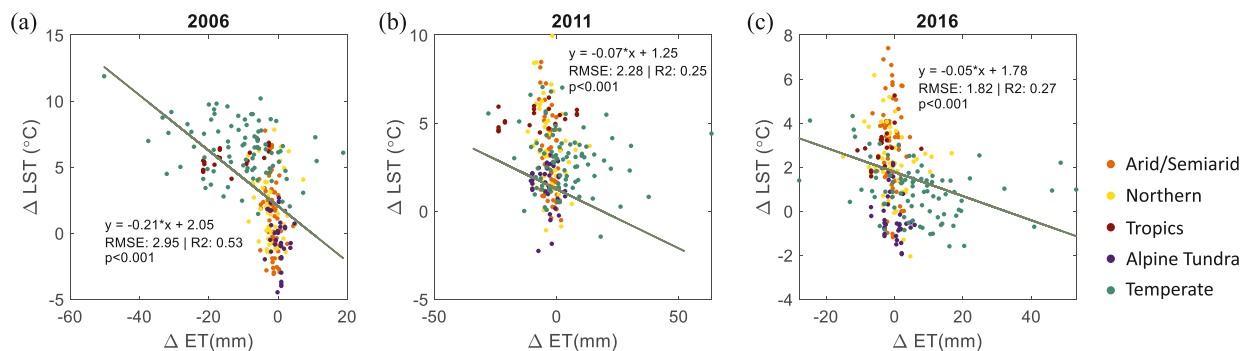


Fig. 16. Fitting annual land surface temperature change (Δ LST) with annual evapotranspiration change (Δ ET) in 2006, 2011, and 2016. The dots with different colors refer to sampled evergreen sites in different climate zones. The grey line represents the relationship between Δ LST and Δ ET. The trend of the grey line suggests how Δ ET is related to Δ LST. R^2 denotes how much variation in Δ LST has been explained by Δ ET. Pixels with insufficient observations are masked out (as we described in Section 2.4.5).

The increased annual Δ Albedo accompanied by the increased annual Δ LAI in the tropics was also reported by Alibakhshi et al. (2020), who indicated that the relationship between albedo and LAI varied over geographical locations. Therefore, additional efforts with field observations are necessary to determine the underlying mechanisms responsible for this relationship.

4.2. Impacts of forest loss on LST

Forest loss generated local cooling in the alpine tundra but resulted in long-term local warming in the arid/semiarid, northern, tropical, and temperate climate zones, though with discrepancies (Figs. 4, 5). However, from the perspective of seasonal Δ LST, negative winter Δ LST was observed in the arid/semiarid and northern evergreen forests, as well as the northern deciduous forests (Fig. 5). Because most of the sampled sites in the arid/semiarid and northern regions are located at higher latitudes, the increase in bare land from forest loss not only facilitated snow accumulation but also reduced the melt rate (Gelfan et al., 2004), thereby contributing to enhanced winter albedo. Besides, the ET reduction in the arid/semiarid and northern regions was less prominent than in the tropical and temperate regions (Fig. 11), so the coupling effect in the winter was dominated by albedo cooling in northern latitudes (Jackson et al., 2008).

The winter cooling at higher latitudes in this study echoes model-dependent experiments (Davin and de Noblet-Ducoudré, 2010; Lorant et al., 2014; van der Molen et al., 2011) and observation-driven assessments (Alkama and Cescatti, 2016; Bonan, 2008; Duveiller et al., 2018; Lee et al., 2011; Zhao and Jackson, 2014). For annual LST, however, we find inconsistent results compared to previous studies. For instance, Alkama and Cescatti (2016) demonstrated annual cooling after forest loss at latitudes north of 50°N in North America, while Duveiller et al. (2018) and Li et al. (2015) suggested that forest loss resulted in decreased mean LST from mid-latitudes. In this study, post-disturbance LST with 30-m spatial resolution indicates the annual warming in the northern sample sites with the maximum latitude at 48.917°N.

4.3. Driving effects of Δ ET and precipitation on local LST associated with forest loss

Forests generally have lower albedo than adjacent open lands. Therefore, with forest loss, increased albedo contributes to less absorption of incoming solar radiation and cooler LST. Meanwhile, the latent heat loss due to decreased ET counteracts the albedo-induced RF. The sign and magnitude of the Δ LST depend mainly on those two biophysical processes. From the relationships between Δ LST with Δ Albedo and Δ ET, respectively, enhanced LST is related to decreased ET (Fig. 16) but increased albedo (Fig. 15a–c). This suggests that the cooling effect of increased albedo can be offset by the warming effect of reduced ET, though previous studies demonstrate contradicting results across northern region (Alkama and Cescatti, 2016; Davin and de Noblet-Ducoudré, 2010; Duveiller et al., 2018; Lee et al., 2011; Li et al., 2015).

From the stepwise fit for Δ LST (Section 3.6.3), Δ Albedo shows more variation relative to Δ LST than that of Δ ET, but the role of Δ Albedo in predicting Δ LST should be concluded carefully. The stepwise fit for Δ LST suggests a positive relationship between Δ Albedo and Δ LST, contradicting the biophysical mechanism that increased albedo contributes to reduced radiative energy flux and ideally leads to local cooling if other land surface variables remain constant. Because post-disturbance Δ LST in a local scale is dominated by Δ Albedo and Δ ET, the resultant local warming highlights that the decreased-ET-induced warming offsets the increased-albedo-induced cooling. The abovementioned process is not observed through stepwise fit for Δ LST due to the following reasons. First, Δ Albedo and Δ ET are not independent from each other. Albedo is a direct measurement, but remote sensing ET is a model product instead of ground observation, and albedo is used as input to predict ET in the MOD16A2 product (Mu et al., 2011). Besides, albedo is generated at

30 m spatial resolution, while ET is at 500 m spatial resolution. The coarser resolution in ET data adds noise when fitting post-disturbance Δ LST. Therefore, the results from stepwise fit for Δ LST should be interpreted carefully.

The confounding effects of Δ Albedo and Δ ET on Δ LST are closely related to precipitation. Specifically, the tropics and the temperate regions experienced stronger and longer post-disturbance warming (Figs. 4, 5), resulting from prominent ET reduction in those two regions (Figs. 10, 11), and were accompanied by greater annual precipitation (Fig. 14). But for the climate zones with lower precipitation, such as the arid/semiarid, the northern, and the alpine tundra (Fig. 14), moderate ET reduction was detected, even slightly enhanced ET in some regions (Figs. 10, 11). It led to relatively weak warming in the arid/semiarid and the northern regions, as well as local cooling in the alpine tundra (Figs. 4, 5). The extent of ET reduction is also determined by how transpiration and evaporation change after forest loss; this is beyond the scope of this research but should be explored in further studies.

4.4. Uncertainties

This study provides new evidence of the biophysical effect of forest loss on LST and identifies the key role of decreased-ET-induced warming on post-disturbance LST. However, uncertainties can still be identified.

4.4.1. Uncertainties from coarser spatial resolution of ET data

The ET from MOD16A2 (V006) is improved by Mu et al. (2011). In contrast with the old algorithm where stomatal conductance shares a constant value across all biomes, the new algorithm allows the mean potential stomatal conductance per unit leaf area to vary with different land cover types. Land cover changes are taken into consideration when specifying the biome physiological parameters (e.g., stomatal conductance) in the MOD16A2 (V006) as the MODIS land cover product used in the improved algorithm is a three-year smoothed land cover dataset (MCDLCHKM) (Running et al., 2019). Therefore, we consider that the MOD16A2 (V006) data is qualified to provide ET data in studies concerning land cover changes. However, the coarser spatial resolution of MOD16A2 (500 m \times 500 m) brings about a potential issue of inconsistent forest type surrounding the sampled 3 \times 3 image chips from the Landsat dataset. Because the pixels that meet the existing masking criteria (i.e., forests that only experience forest loss in 2005 and the vegetation type is consistent before and after the forest loss) are quite discrete, and the further requirement of similar surrounding vegetation types ends up with an empty result of sample sites in all the five climate zones, we compromise on a less parsimonious mask that sets the surrounding pixels as forest instead of the same forest type. Potential uncertainties should be considered when using ET and LAI from the MODIS 500 m product to represent the corresponding variable in pixels with a finer resolution.

4.4.2. Uncertainties from the lack of field data validation

Field data validation, if available, will help ensure that the remote sensing products or meteorological datasets used in this study are robust. However, we have little concern about the uncertainty caused by the lack of field data validation, because the remote sensing products and meteorological datasets used here have been carefully examined in previous studies. Specifically, the LST algorithm has been validated by Ermida et al. (2020) using in-situ LST in 12 stations. They found a good agreement between Landsat LST and in-situ LST. Similarly, the algorithm used to derive land surface albedo has been validated by Liang et al. (2003) using field data at one of 24 NASA EOS (Earth Observing System) Land Core Validation Sites. They suggested a good consistency between filed data and Landsat-derived shortwave albedo. Other products used in this study (i.e., evapotranspiration, leaf area index, and precipitation) have also been validated (Mu et al., 2011; Myneni et al., 2015; Thornton et al., 2017) and extensively used in related works

(Hao et al., 2021; Holden et al., 2018; Hu et al., 2021; Maness et al., 2013; Meng et al., 2020; Vanderhoof and Williams, 2015; Wang et al., 2016; Zhou et al., 2018).

4.4.3. Uncertainties from not considering the variation of surface roughness

This study focuses on the response of post-disturbance local LST to two major biophysical processes (i.e., albedo and ET), but the local warming attributed to decreased surface roughness should also be noted. Though previous studies suggested that the biophysical temperature effects of deforestation are mainly controlled by changes in albedo and evapotranspiration (Bala et al., 2007; Li et al., 2015; Liu et al., 2019; Prevedello et al., 2019), the variation of surface roughness also regulates the post-disturbance LST in addition to albedo and ET. Some studies recognized the importance of surface roughness (Khanna and Medvigy, 2014; Yuan et al., 2021), and even considered surface roughness as a key driver for local changes in surface temperature (Chen and Dirmeyer, 2016; Davin and de Noblet-Ducoudré, 2010; Lee et al., 2011; Winckler et al., 2017). With deforestation, decreased surface roughness tends to reduce turbulent exchanges. The weakened turbulent exchanges cannot transfer the energy available at the surface to the atmosphere, thus leading to local warming (Bonan, 2015; Davin and de Noblet-Ducoudré, 2010).

5. Conclusions

Biophysical effects of forest loss on LST have been extensively studied on local and global scales, but to the best of our knowledge, few large-scale studies have been conducted with fine spatial resolution. Space-for-time substitution used in most studies treats the current vegetation at control sites as a substitute for pre-disturbance vegetation, ignoring the vegetation difference between disturbed sites and control sites and the interannual variation in vegetation that is not caused by forest loss, but by natural growth or background climate. We adopted a synergetic approach to minimize the abovementioned concerns. Specifically, we subtracted the trend detected at control sites from the time series at disturbed sites; the remaining signal allowed comparison before and after forest loss to evaluate the pure impact of forest loss on the land surface variables.

We investigated how forest loss affected LST through biophysical processes with 30 m spatial resolution data. Increased albedo was observed at all the disturbed sites, and its cooling effect was counteracted by decreased-ET-induced warming in the arid/semiarid, northern, tropical, and temperate regions, leading to net annual warming. Though the stepwise fit for Δ LST suggests that Δ Albedo plays a key role in fitting Δ LST, it contradicts the biophysical mechanism that increased albedo leads to local cooling, therefore should be interpreted with caution. From the perspective of seasonal Δ LST, the sample sites in the arid/semiarid evergreen and northern forests (i.e., the evergreen and deciduous) experienced winter cooling. Besides, the confounding effects of Δ Albedo and Δ ET on Δ LST were closely related to precipitation. The climate zones with greater precipitation (i.e., the tropical and the temperate) experienced stronger and longer warming after forest loss due to larger ET reduction, whereas the climate zones with less precipitation (i.e., the arid/semiarid, the alpine tundra, and the northern) experienced mild local warming or even local cooling, accompanied by lower ET reduction or even slightly increased ET. Forest loss decreased LAI in all the five climate zones, with stronger impacts on the evergreen than on the deciduous forests. Δ LAI suggests continuous forest recovery in the tropical, temperate, and northern regions, but it has limited help in explaining the post-disturbance Δ LST because the forest recovery inferred by LAI does not necessarily synchronize with the recovery of albedo or ET. Overall, this study explores biophysical effects of forest loss on local LST, identifying the key role of decreased-ET-induced warming after deforestation.

CRedit authorship contribution statement

Yang Li: Conceptualization, Methodology, Validation, Formal analysis, Data curation, Writing – original draft. **Yanlan Liu:** Supervision, Methodology, Formal analysis, Writing – review & editing. **Gil Bohrer:** Supervision, Methodology, Formal analysis, Writing – review & editing. **Yongyang Cai:** Supervision, Writing – review & editing. **Aaron Wilson:** Conceptualization, Writing – review & editing. **Tongxi Hu:** Visualization, Writing – review & editing. **Zhihao Wang:** Investigation, Writing – review & editing. **Kaiguang Zhao:** Supervision, Conceptualization, Methodology, Investigation, Formal analysis, Funding acquisition, Writing – review & editing.

Declaration of competing interest

The authors declare that they have no known competing financial interests or personal relationships that could have appeared to influence the work reported in this paper.

Acknowledgments

We gratefully acknowledge the support from the USDA Agricultural Research Service (grant nos. 2018-68002-27932). We also thank Elena Paoletti and three anonymous reviewers for their constructive comments.

Appendix A. Supplementary information

Supplementary data to this article can be found online at <https://doi.org/10.1016/j.scitotenv.2021.149651>.

References

- Alibakhshi, S., Naimi, B., Hovi, A., Crowther, T.W., Rautiainen, M., 2020. Quantitative analysis of the links between forest structure and land surface albedo on a global scale. *Remote Sens. Environ.* 246, 111854. <https://doi.org/10.1016/j.rse.2020.111854>.
- Alix-Garcia, J., Wolff, H., 2014. Payment for ecosystem services from forests. *Annu. Rev. Resour. Econ.* 6, 361–380. <https://doi.org/10.1146/annurev-resource-100913-012524>.
- Alkama, R., Cescatti, A., 2016. Biophysical climate impacts of recent changes in global forest cover. *Science* 351, 600–604. <https://doi.org/10.1126/science.aac8083>.
- Allen, C.D., Macalady, A.K., Chenchouni, H., Bachelet, D., McDowell, N., Vennetier, M., Kitzberger, T., Rigling, A., Breshears, D.D., Hogg, E.H., (Ted) P., Gonzalez, 2010. A global overview of drought and heat-induced tree mortality reveals emerging climate change risks for forests. *Forest Ecology and Management, Adaptation of Forests and Forest Management to Changing Climate*. 259, pp. 660–684. <https://doi.org/10.1016/j.foreco.2009.09.001>.
- Amiro, B.D., Barr, A.G., Barr, J.G., Black, T.A., Bracho, R., Brown, M., Chen, J., Clark, K.L., Davis, K.J., Desai, A.R., Dore, S., Engel, V., Fuentes, J.D., Goldstein, A.H., Goulden, M.L., Kolb, T.E., Lavigne, M.B., Law, B.E., Margolis, H.A., Martin, T., McCaughey, J.H., Misson, L., Montes-Helu, M., Noormets, A., Randerson, J.T., Starr, G., Xiao, J., 2010. Ecosystem carbon dioxide fluxes after disturbance in forests of North America. *J. Geophys. Res. Biogeosci.* 115. <https://doi.org/10.1029/2010JG001390>.
- Anderson, R.G., Canadell, J.G., Randerson, J.T., Jackson, R.B., Hungate, B.A., Baldocchi, D.D., Ban-Weiss, G.A., Bonan, G.B., Caldeira, K., Cao, L., Diffenbaugh, N.S., Gurney, K.R., Kueppers, L.M., Law, B.E., Luyssaert, S., O'Halloran, T.L., 2011. Biophysical considerations in forestry for climate protection. *Front. Ecol. Environ.* 9, 174–182. <https://doi.org/10.1890/090179>.
- Anderson-Teixeira, K.J., Miller, A.D., Mohan, J.E., Hudiburg, T.W., Duval, B.D., DeLucia, E.H., 2013. Altered dynamics of forest recovery under a changing climate. *Glob. Chang. Biol.* 19, 2001–2021. <https://doi.org/10.1111/gcb.12194>.
- Bala, G., Caldeira, K., Wickett, M., Phillips, T.J., Lobell, D.B., Delire, C., Mirin, A., 2007. Combined climate and carbon-cycle effects of large-scale deforestation. *PNAS* 104, 6550–6555. <https://doi.org/10.1073/pnas.060898104>.
- Banerjee, T., De Roo, F., Mauder, M., 2017. Explaining the convective effect in canopy turbulence by means of large-eddy simulation. *Hydrol. Earth Syst. Sci.* 21, 2987–3000. <https://doi.org/10.5194/hess-21-2987-2017>.
- Barlow, J., Lennox, G.D., Ferreira, J., Berenguer, E., Lees, A.C., Nally, R.M., Thomson, J.R., de Ferraz, S.F., B. J., Louzada, 2016. Anthropogenic disturbance in tropical forests can double biodiversity loss from deforestation. *Nature* 535, 144–147. <https://doi.org/10.1038/nature18326>.
- Barnes, C.A., Roy, D.P., 2008. Radiative forcing over the conterminous United States due to contemporary land cover land use albedo change. *Geophys. Res. Lett.* 35. <https://doi.org/10.1029/2008GL033567>.

- Beck, H.E., Zimmermann, N.E., McVicar, T.R., Vergopolan, N., Berg, A., Wood, E.F., 2018. Present and future Köppen-Geiger climate classification maps at 1-km resolution. *Sci. Data* 5, 180214. <https://doi.org/10.1038/sdata.2018.214>.
- Bonan, G.B., 2008. Forests and climate change: forcings, feedbacks, and the climate benefits of forests. *Science* 320, 1444–1449. <https://doi.org/10.1126/science.1155121>.
- Bonan, G., 2015. *Ecological Climatology: Concepts and Applications*. Third ed. Cambridge University Press, Cambridge, UK.
- Bond-Lamberty, B., Peckham, S.D., Gower, S.T., Ewers, B.E., 2009. Effects of fire on regional evapotranspiration in the central Canadian boreal forest. *Glob. Chang. Biol.* 15, 1242–1254. <https://doi.org/10.1111/j.1365-2486.2008.01776.x>.
- Bounoua, L., DeFries, R., Collatz, G.J., Sellers, P., Khan, H., 2002. Effects of land cover conversion on surface climate. *Clim. Chang.* 52, 29–64. <https://doi.org/10.1023/A:1013051420309>.
- Bright, R.M., Zhao, K., Jackson, R.B., Cherubini, F., 2015. Quantifying surface albedo and other direct biogeophysical climate forcings of forestry activities. *Glob. Chang. Biol.* 21, 3246–3266. <https://doi.org/10.1111/gcb.12951>.
- Bright, R.M., Davin, E., O'Halloran, T., Pongratz, J., Zhao, K., Cescatti, A., 2017. Local temperature response to land cover and management change driven by non-radiative processes. *Nat. Clim. Chang.* 7, 296–302. <https://doi.org/10.1038/nclimate3250>.
- Burakowski, E., Tawfik, A., Ouimette, A., Lepine, L., Novick, K., Ollinger, S., Zarzycki, C., Bonan, G., 2018. The role of surface roughness, albedo, and Bowen ratio on ecosystem energy balance in the Eastern United States. *Agric. For. Meteorol.* 249, 367–376. <https://doi.org/10.1016/j.agrformet.2017.11.030>.
- Chapman, E.L., Chambers, J.Q., Ribbeck, K.F., Baker, D.B., Tobler, M.A., Zeng, H., White, D.A., 2008. Hurricane Katrina impacts on forest trees of Louisiana's Pearl River basin. *For. Ecol. Manag.* 256, 883–889. <https://doi.org/10.1016/j.foreco.2008.05.057>.
- Chen, L., Dirmeyer, P.A., 2016. Adapting observationally based metrics of biogeophysical feedbacks from land cover/land use change to climate modeling. *Environ. Res. Lett.* 11, 034002. <https://doi.org/10.1088/1748-9326/11/3/034002>.
- Chen, C.-F., Lau, V.-K., Chang, N.-B., Son, N.-T., Tong, P.-H.-S., Chiang, S.-H., 2016. Multi-temporal change detection of seagrass beds using integrated landsat TM/ETM+/OLI imageries in Cam Ranh Bay, Vietnam. *Ecol. Inf.* 35, 43–54. <https://doi.org/10.1016/j.ecoinf.2016.07.005>.
- Claverie, M., Vermote, E.F., Franch, B., Masek, J.G., 2015. Evaluation of the Landsat-5 TM and Landsat-7 ETM+ surface reflectance products. *Remote Sens. Environ.* 169, 390–403. <https://doi.org/10.1016/j.rse.2015.08.030>.
- Cosgrove, B.A., Lohmann, D., Mitchell, K.E., Houser, P.R., Wood, E.F., Schaake, J.C., Robock, A., Marshall, C., Sheffield, J., Duan, Q., Luo, L., Higgins, R.W., Pinker, R.T., Tarpley, J.D., Meng, J., 2003. Real-time and retrospective forcing in the North American Land Data Assimilation System (NLDAS) project. *J. Geophys. Res. Atmos.* 108. <https://doi.org/10.1029/2002JD003118>.
- Davin, E.L., de Noblet-Ducoudré, N., 2010. Climatic impact of global-scale deforestation: radiative versus nonradiative processes. *J. Clim.* 23, 97–112. <https://doi.org/10.1175/2009JCLI3102.1>.
- de Oliveira, J.V., Ferreira, D.B.da S., Sahoo, P.K., Sodré, G.R.C., de Souza, E.B., Queiroz, J.C.B., 2018. Differences in precipitation and evapotranspiration between forested and deforested areas in the Amazon rainforest using remote sensing data. *Environ. Earth Sci.* 77, 239. <https://doi.org/10.1007/s12665-018-7411-9>.
- DeBortoli, N.S., Dubreuil, V., Hirota, M., Filho, S.R., Lindoso, D.P., Nabucet, J., 2017. Detecting deforestation impacts in southern Amazonia rainfall using rain gauges. *Int. J. Climatol.* 37, 2889–2900. <https://doi.org/10.1002/joc.4886>.
- Delzon, S., Loustau, D., 2005. Age-related decline in stand water use: sap flow and transpiration in a pine forest chronosequence. *Agric. For. Meteorol.* 129, 105–119. <https://doi.org/10.1016/j.agrformet.2005.01.002>.
- Duveiller, G., Hooker, J., Cescatti, A., 2018. The mark of vegetation change on Earth's surface energy balance. *Nat. Commun.* 9, 679. <https://doi.org/10.1038/s41467-017-02810-8>.
- Eder, F., De Roo, F., Rotenberg, E., Yakir, D., Schmid, H.P., Mauder, M., 2015. Secondary circulations at a solitary forest surrounded by semi-arid shrubland and their impact on eddy-covariance measurements. *Agric. For. Meteorol.* 211–212, 115–127. <https://doi.org/10.1016/j.agrformet.2015.06.001>.
- Ellenburg, W.L., McNider, R.T., Cruise, J.F., Christy, J.R., 2016. Towards an understanding of the twentieth-century cooling trend in the southeastern United States: biogeophysical impacts of land-use change. *Earth Interact.* 20, 1–31. <https://doi.org/10.1175/EI-D-15-0038.1>.
- Ermida, S.L., Soares, P., Mantas, V., Göttsche, F.-M., Trigo, I.F., 2020. Google Earth Engine open-source code for land surface temperature estimation from the Landsat series. *Remote Sens.* 12, 1471. <https://doi.org/10.3390/rs12091471>.
- Flood, N., 2014. Continuity of reflectance data between Landsat-7 ETM+ and Landsat-8 OLI, for both top-of-atmosphere and surface reflectance: a study in the Australian landscape. *Remote Sens.* 6, 7952–7970. <https://doi.org/10.3390/rs6097952>.
- Gelfan, A.N., Pomeroy, J.W., Kuchment, L.S., 2004. Modeling forest cover influences on snow accumulation, sublimation, and melt. *J. Hydrometeorol.* 5, 785–803. [https://doi.org/10.1175/1525-7541\(2004\)005<0785:MFCIOS>2.0.CO;2](https://doi.org/10.1175/1525-7541(2004)005<0785:MFCIOS>2.0.CO;2).
- Gibbs, H.K., Herold, M., 2007. Tropical deforestation and greenhouse gas emissions. *Environ. Res. Lett.* 2, 045021. <https://doi.org/10.1088/1748-9326/2/4/045021>.
- Goetz, S.J., Mack, M.C., Gurney, K.R., Randerson, J.T., Houghton, R.A., 2007. Ecosystem responses to recent climate change and fire disturbance at northern high latitudes: observations and model results contrasting northern Eurasia and North America. *Environ. Res. Lett.* 2, 045031. <https://doi.org/10.1088/1748-9326/2/4/045031>.
- Gorelick, N., Hancher, M., Dixon, M., Ilyushchenko, S., Thau, D., Moore, R., 2017. Google Earth Engine: planetary-scale geospatial analysis for everyone. *Remote Sensing of Environment, Big Remotely Sensed Data: Tools, Applications and Experiences*. 202, pp. 18–27. <https://doi.org/10.1016/j.rse.2017.06.031>.
- Griffiths, P., Kuemmerle, T., Baumann, M., Radeloff, V.C., Abrudan, I.V., Lieskovsky, J., Munteanu, C., Ostapowicz, K., Hostert, P., 2014. Forest disturbances, forest recovery, and changes in forest types across the Carpathian ecoregion from 1985 to 2010 based on Landsat image composites. *Remote Sensing of Environment, Special Issue on 2012 ForestSAT*. 151, pp. 72–88. <https://doi.org/10.1016/j.rse.2013.04.022>.
- Hansen, J., Sato, M., Ruedy, R., 1997. Radiative forcing and climate response. *J. Geophys. Res. Atmos.* 102, 6831–6864. <https://doi.org/10.1029/96JD03436>.
- Hansen, J., Sato, M., Ruedy, R., Lo, K., Lea, D.W., Medina-Elizade, M., 2006. Global temperature change. *PNAS* 103, 14288–14293. <https://doi.org/10.1073/pnas.0606291103>.
- Hansen, M.C., Potapov, P.V., Moore, R., Hancher, M., Turubanova, S.A., Tyukavina, A., Thau, D., Stehman, S.V., Goetz, S.J., Loveland, T.R., Kommareddy, A., Egorov, A., Chini, L., Justice, C.O., Townshend, J.R.G., 2013. High-resolution global maps of 21st-century forest cover change. *Science* 342, 850–853. <https://doi.org/10.1126/science.1244693>.
- Hao, D., Asrar, G.R., Zeng, Y., Yang, X., Li, X., Xiao, J., Guan, K., Wen, J., Xiao, Q., Berry, J.A., Chen, M., 2021. Potential of hotspot solar-induced chlorophyll fluorescence for better tracking terrestrial photosynthesis. *Glob. Chang. Biol.* 27, 2144–2158. <https://doi.org/10.1111/gcb.15554>.
- He, T., Liang, S., Wang, D., Cao, Y., Gao, F., Yu, Y., Feng, M., 2018. Evaluating land surface albedo estimation from landsat MSS, TM, ETM+, and OLI data based on the unified direct estimation approach. *Remote Sens. Environ.* 204, 181–196. <https://doi.org/10.1016/j.rse.2017.10.031>.
- Hirano, T., Suzuki, K., Hirata, R., 2017. Energy balance and evapotranspiration changes in a larch forest caused by severe disturbance during an early secondary succession. *Agric. For. Meteorol.* 232, 457–468. <https://doi.org/10.1016/j.agrformet.2016.10.003>.
- Holden, Z.A., Swanson, A., Luce, C.H., Jolly, W.M., Maneta, M., Oyler, J.W., Warren, D.A., Parsons, R., Affleck, D., 2018. Decreasing fire season precipitation increased recent western US forest wildfire activity. *PNAS* 115, E8349–E8357. <https://doi.org/10.1073/pnas.1802316115>.
- Homer, C., Dewitz, J., Jin, S., Xian, G., Costello, C., Danielson, P., Gass, L., Funk, M., Wickham, J., Stehman, S., Auch, R., Riitters, K., 2020. Conterminous United States land cover change patterns 2001–2016 from the 2016 National Land Cover Database. *ISPRS J. Photogramm. Remote Sens.* 162, 184–199. <https://doi.org/10.1016/j.isprsjprs.2020.02.019>.
- Hooker, J., Duveiller, G., Cescatti, A., 2018. A global dataset of air temperature derived from satellite remote sensing and weather stations. *Sci. Data* 5, 180246. <https://doi.org/10.1038/sdata.2018.246>.
- Hu, T., Myers Toman, E., Chen, G., Shao, G., Zhou, Y., Li, Y., Zhao, K., Feng, Y., 2021. Mapping fine-scale human disturbances in a working landscape with Landsat time series on Google Earth Engine. *ISPRS J. Photogramm. Remote Sens.* 176, 250–261. <https://doi.org/10.1016/j.isprsjprs.2021.04.008>.
- Hubbard, R.M., Rhoades, C.C., Elder, K., Negron, J., 2013. Changes in transpiration and foliage growth in lodgepole pine trees following mountain pine beetle attack and mechanical girdling. *For. Ecol. Manag.* 289, 312–317. <https://doi.org/10.1016/j.foreco.2012.09.028>.
- Jackson, R.B., Jobbágy, E.G., Avissar, R., Roy, S.B., Barrett, D.J., Cook, C.W., Farley, K.A., le Maitre, D.C., McCarl, B.A., Murray, B.C., 2005. Trading water for carbon with biological carbon sequestration. *Science* 310, 1944–1947. <https://doi.org/10.1126/science.1119282>.
- Jackson, R.B., Randerson, J.T., Canadell, J.G., Anderson, R.G., Avissar, R., Baldocchi, D.D., Bonan, G.B., Caldeira, K., Diffenbaugh, N.S., Field, C.B., Hungate, B.A., Jobbágy, E.G., Kueppers, L.M., Nozotto, M.D., Pataki, D.E., 2008. Protecting climate with forests. *Environ. Res. Lett.* 3, 044006. <https://doi.org/10.1088/1748-9326/3/4/044006>.
- Jarvis, A., Reuter, H.I., Nelson, A., Guevara, E., 2008. Hole-filled SRTM for the globe version 4. <http://srtm.csi.cgiar.org> available from the CGIAR-CSI SRTM 90m database.
- Jiang, L., Jiapaer, G., Bao, A., Li, Y., Guo, H., Zheng, G., Chen, T., De Maeyer, P., 2019. Assessing land degradation and quantifying its drivers in the Amudarya River delta. *Ecol. Indic.* 107, 105595. <https://doi.org/10.1016/j.ecolind.2019.105595>.
- Jiang, Y., Wang, G., Liu, W., Erfanian, A., Peng, Q., Fu, R., 2021. Modeled response of South American climate to three decades of deforestation. *J. Clim.* 34, 2189–2203. <https://doi.org/10.1175/JCLI-D-20-0380.1>.
- Jiao, T., Williams, C.A., Ghimire, B., Masek, J., Gao, F., Schaaf, C., 2017. Global climate forcing from albedo change caused by large-scale deforestation and reforestation: quantification and attribution of geographic variation. *Clim. Chang.* 142, 463–476. <https://doi.org/10.1007/s10584-017-1962-8>.
- Jin, M., Dickinson, R.E., 2010. Land surface skin temperature climatology: benefitting from the strengths of satellite observations. *Environ. Res. Lett.* 5, 044004. <https://doi.org/10.1088/1748-9326/5/4/044004>.
- Jin, Y., Roy, D.P., 2005. Fire-induced albedo change and its radiative forcing at the surface in northern Australia. *Geophys. Res. Lett.* 32. <https://doi.org/10.1029/2005GL022822>.
- Jin, S., Homer, C., Yang, L., Danielson, P., Dewitz, J., Li, C., Zhu, Z., Xian, G., Howard, D., 2019. Overall methodology design for the United States National Land Cover Database 2016 products. *Remote Sens.* 11, 2971. <https://doi.org/10.3390/rs11242971>.
- Kang, S., Kimball, J.S., Running, S.W., 2006. Simulating effects of fire disturbance and climate change on boreal forest productivity and evapotranspiration. *Sci. Total Environ.* 362, 85–102. <https://doi.org/10.1016/j.scitotenv.2005.11.014>.
- Kennedy, R.E., Yang, Z., Cohen, W.B., Pfaff, E., Braaten, J., Nelson, P., 2012. Spatial and temporal patterns of forest disturbance and regrowth within the area of the northwest Forest Plan. *Remote Sensing of Environment, Landsat Legacy Special Issue*. 122, pp. 117–133. <https://doi.org/10.1016/j.rse.2011.09.024>.
- Khanna, J., Medvigy, D., 2014. Strong control of surface roughness variations on the simulated dry season regional atmospheric response to contemporary deforestation in Rondônia, Brazil. *J. Geophys. Res. Atmos.* 119, 13067–13078. <https://doi.org/10.1002/2014JD022278>.
- Kvalevåg, M.M., Myhre, G., Bonan, G., Levis, S., 2010. Anthropogenic land cover changes in a GCM with surface albedo changes based on MODIS data. *Int. J. Climatol.* 30, 2105–2117. <https://doi.org/10.1002/joc.2012>.
- Lagué, M.M., Bonan, G.B., Swann, A.L.S., 2019. Separating the impact of individual land surface properties on the terrestrial surface energy budget in both the coupled and

- uncoupled land-atmosphere system. *J. Clim.* 32, 5725–5744. <https://doi.org/10.1175/JCLI-D-18-0812.1>.
- Landry, J.-S., Parrott, L., Price, D.T., Ramankutty, N., Matthews, H.D., 2016. Modelling long-term impacts of mountain pine beetle outbreaks on merchantable biomass, ecosystem carbon, albedo, and radiative forcing. *Biogeosciences* 13, 5277–5295. <https://doi.org/10.5194/bg-13-5277-2016>.
- Lane, P.N.J., Mackay, S.M., 2001. Streamflow response of mixed-species eucalypt forests to patch cutting and thinning treatments. *For. Ecol. Manag.* 143, 131–142. [https://doi.org/10.1016/S0378-1127\(00\)00512-0](https://doi.org/10.1016/S0378-1127(00)00512-0).
- Lawrence, D., Vandecar, K., 2015. Effects of tropical deforestation on climate and agriculture. *Nat. Clim. Chang.* 5, 27–36. <https://doi.org/10.1038/nclimate2430>.
- Lean, J., Warrilow, D.A., 1989. Simulation of the regional climatic impact of Amazon deforestation. *Nature* 342, 411–413. <https://doi.org/10.1038/342411a0>.
- Lee, X., Goulden, M.L., Hollinger, D.Y., Barr, A., Black, T.A., Bohrer, G., Bracho, R., Drake, B., Goldstein, A., Gu, L., Katul, G., Kolb, T., Law, B.E., Margolis, H., Meyers, T., Monson, R., Munger, W., Oren, R., Paw U, K.T., Richardson, A.D., Schmid, H.P., Staebler, R., Wofsy, S., Zhao, L., 2011. Observed increase in local cooling effect of deforestation at higher latitudes. *Nature* 479, 384–387. <https://doi.org/10.1038/nature10588>.
- Lejeune, Q., Davin, E.L., Guillod, B.P., Seneviratne, S.I., 2015. Influence of Amazonian deforestation on the future evolution of regional surface fluxes, circulation, surface temperature and precipitation. *Clim. Dyn.* 44, 2769–2786. <https://doi.org/10.1007/s00382-014-2203-8>.
- Li, Z.-L., Tang, B.-H., Wu, H., Ren, H., Yan, G., Wan, Z., Trigo, I.F., Sobrino, J.A., 2013. Satellite-derived land surface temperature: current status and perspectives. *Remote Sens. Environ.* 131, 14–37. <https://doi.org/10.1016/j.rse.2012.12.008>.
- Li, Y., Zhao, M., Motesharrei, S., Mu, Q., Kalnay, E., Li, S., 2015. Local cooling and warming effects of forests based on satellite observations. *Nat. Commun.* 6, 6603. <https://doi.org/10.1038/ncomms7603>.
- Li, Y., Guan, K., Peng, B., Franz, T.E., Wardlow, B., Pan, M., 2020. Quantifying irrigation cooling benefits to maize yield in the US Midwest. *Glob. Chang. Biol.* 26, 3065–3078. <https://doi.org/10.1111/gcb.15002>.
- Liang, S., 2001. Narrowband to broadband conversions of land surface albedo I: algorithms. *Remote Sens. Environ.* 76, 213–238. [https://doi.org/10.1016/S0034-4257\(00\)00205-4](https://doi.org/10.1016/S0034-4257(00)00205-4).
- Liu, Y., Parolari, A.J., Kumar, M., Huang, C.-W., Katul, G.G., Porporato, A., 2017. Increasing atmospheric humidity and CO₂ concentration alleviate forest mortality risk. *PNAS* 114, 9918–9923. <https://doi.org/10.1073/pnas.1704811114>.
- Liang, S., Shuey, C.J., Russ, A.L., Fang, H., Chen, M., Walthall, C.L., Daughtry, C.S., Hunt Jr, R., 2003. Narrowband to broadband conversions of land surface albedo: II. Validation. *Remote Sens. Environ.* 84 (1), 25–41. [https://doi.org/10.1016/S0034-4257\(02\)00068-8](https://doi.org/10.1016/S0034-4257(02)00068-8).
- Liu, Z., Ballantyne, A.P., Cooper, L.A., 2019. Biophysical feedback of global forest fires on surface temperature. *Nat. Commun.* 10, 214. <https://doi.org/10.1038/s41467-018-08237-z>.
- Liu, Y., Kumar, M., Katul, G.G., Feng, X., Konings, A.G., 2020. Plant hydraulics accentuates the effect of atmospheric moisture stress on transpiration. *Nat. Clim. Chang.* 10, 691–695. <https://doi.org/10.1038/s41558-020-0781-5>.
- Lorant, M.M., Berner, L.T., Goetz, S.J., Jin, Y., Randerson, J.T., 2014. Vegetation controls on northern high latitude snow-albedo feedback: observations and CMIP5 model simulations. *Glob. Chang. Biol.* 20, 594–606. <https://doi.org/10.1111/gcb.12391>.
- Luo, L., Robock, A., Mitchell, K.E., Houser, P.R., Wood, E.F., Schaake, J.C., Lohmann, D., Cosgrove, B., Wen, F., Sheffield, J., Duan, Q., Higgins, R.W., Pinker, R.T., Tarpley, J.D., 2003. Validation of the North American Land Data Assimilation System (NLDAS) retrospective forcing over the northern Great Plains. *J. Geophys. Res. Atmos.* 108. <https://doi.org/10.1029/2002JD003246>.
- Ma, Q., Bales, R.C., Runge, J., Conklyn, M.H., Collins, B.M., Goulden, M.L., 2020. Wildfire controls on evapotranspiration in California's Sierra Nevada. *J. Hydrol.* 590, 125364. <https://doi.org/10.1016/j.jhydrol.2020.125364>.
- Maness, H., Kushner, P.J., Fung, I., 2013. Summertime climate response to mountain pine beetle disturbance in British Columbia. *Nat. Geosci.* 6, 65–70. <https://doi.org/10.1038/ngeo1642>.
- Martins, J.P.A., Trigo, I.F., Bento, V.A., Da Camara, C., 2016. A physically constrained calibration database for land surface temperature using infrared retrieval algorithms. *Remote Sens.* 8, 808. <https://doi.org/10.3390/rs8100808>.
- Matheny, A.M., Bohrer, G., Vogel, C.S., Morin, T.H., He, L., de Frasson, R.P., M. G., Mirfenderesgi, 2014. Species-specific transpiration responses to intermediate disturbance in a northern hardwood forest. *J. Geophys. Res. Biogeosci.* 119, 2292–2311. <https://doi.org/10.1002/2014JG002804>.
- McAlpine, C., Ryan, J., Seabrook, L., Thomas, S., Dargusch, P., Syktus, J., Pielke, R., Etter, A., Fearnside, P., Laurance, W., 2010. More than CO₂: a broader paradigm for managing climate change and variability to avoid ecosystem collapse. *Curr. Opin. Environ. Sustain.* 2, 334–346. <https://doi.org/10.1016/j.cosust.2010.10.001>.
- Medvigy, D., Walko, R.L., Avissar, R., 2011. Effects of deforestation on spatiotemporal distributions of precipitation in South America. *J. Clim.* 24, 2147–2163. <https://doi.org/10.1175/2010JCLI3882.1>.
- Meng, L., Mao, J., Zhou, Y., Richardson, A.D., Lee, X., Thornton, P.E., Ricciuto, D.M., Li, X., Dai, Y., Shi, X., Jia, G., 2020. Urban warming advances spring phenology but reduces the response of phenology to temperature in the conterminous United States. *PNAS* 117, 4228–4233. <https://doi.org/10.1073/pnas.1911117117>.
- Mikkelsen, K.M., Bearup, L.A., Maxwell, R.M., Stednick, J.D., McCray, J.E., Sharp, J.O., 2013. Bark beetle infestation impacts on nutrient cycling, water quality and interdependent hydrological effects. *Biogeochemistry* 115, 1–21. <https://doi.org/10.1007/s10533-013-9875-8>.
- Mitchell, R.G., Preisler, H.K., 1998. Fall rate of lodgepole pine killed by the mountain pine beetle in Central Oregon. *West. J. Appl. For.* 13, 23–26. <https://doi.org/10.1093/wjaf/13.1.23>.
- Moran, R.J., O'Shaughnessy, P.J., 1984. Determination of the evapotranspiration of E. regnans forested catchments using hydrological measurements. In: Sharma, M.L. (Ed.), *Developments in Agricultural and Managed Forest Ecology, Evapotranspiration from Plant Communities*. Elsevier, pp. 57–76. <https://doi.org/10.1016/B978-0-444-42250-7.50008-2>.
- Mu, Q., Zhao, M., Running, S.W., 2011. Improvements to a MODIS global terrestrial evapotranspiration algorithm. *Remote Sens. Environ.* 115, 1781–1800. <https://doi.org/10.1016/j.rse.2011.02.019>.
- Myneni, R., Knyazikhin, Y., Park, T., 2015. MOD15A2H MODIS/terra Leaf Area Index/FPAR 8-day L4 Global 500 m SIN Grid V006.
- Naegeli, K., Damm, A., Huss, M., Wulf, H., Schaepman, M., Hoelzle, M., 2017. Cross-comparison of albedo products for glacier surfaces derived from airborne and satellite (sentinel-2 and landsat 8) optical data. *Remote Sens.* 9 (2), 110. <https://doi.org/10.3390/rs9020110>.
- Nobre, P., Malagutti, M., Urbano, D.F., de Almeida, R.A.F., Giarolla, E., 2009. Amazon deforestation and climate change in a coupled model simulation. *J. Clim.* 22, 5686–5697. <https://doi.org/10.1175/2009JCLI2757.1>.
- Nolan, R.H., Lane, P.N.J., Benyon, R.G., Bradstock, R.A., Mitchell, P.J., 2015. Trends in evapotranspiration and streamflow following wildfire in resprouting eucalypt forests. *J. Hydrol.* 524, 614–624. <https://doi.org/10.1016/j.jhydrol.2015.02.045>.
- O'Halloran, T.L., Law, B.E., Goulden, M.L., Wang, Z., Barr, J.G., Schaaf, C., Brown, M., Fuentes, J.D., Gökede, M., Black, A., Engel, V., 2012. Radiative forcing of natural forest disturbances. *Glob. Chang. Biol.* 18, 555–565. <https://doi.org/10.1111/j.1365-2486.2011.02577.x>.
- Oliphant, A.J., Thenkabail, P.S., Teluguntla, P., Xiong, J., Gumma, M.K., Congalton, R.G., Yadav, K., 2019. Mapping cropland extent of Southeast and Northeast Asia using multi-year time-series Landsat 30-m data using a random forest classifier on the Google Earth Engine Cloud. *Int. J. Appl. Earth Obs. Geoinf.* 81, 110–124. <https://doi.org/10.1016/j.jag.2018.11.014>.
- Peng, S.-S., Piao, S., Zeng, Z., Ciais, P., Zhou, L., Li, L.Z.X., Myneni, R.B., Yin, Y., Zeng, H., 2014. Afforestation in China cools local land surface temperature. *PNAS* 111, 2915–2919. <https://doi.org/10.1073/pnas.1315126111>.
- Perugini, L., Caporaso, L., Marconi, S., Cescatti, A., Quesada, B., de Noblet-Ducoudré, N., House, J.I., Arneth, A., 2017. Biophysical effects on temperature and precipitation due to land cover change. *Environ. Res. Lett.* 12, 053002. <https://doi.org/10.1088/1748-9326/aa6b3f>.
- Pitman, A.J., Lorenz, R., 2016. Scale dependence of the simulated impact of Amazonian deforestation on regional climate. *Environ. Res. Lett.* 11, 094025. <https://doi.org/10.1088/1748-9326/11/9/094025>.
- Poon, P.K., Kinoshita, A.M., 2018. Spatial and temporal evapotranspiration trends after wildfire in semi-arid landscapes. *J. Hydrol.* 559, 71–83. <https://doi.org/10.1016/j.jhydrol.2018.02.023>.
- Prevedello, J.A., Winck, G.R., Weber, M.M., Nichols, E., Sinervo, B., 2019. Impacts of forestation and deforestation on local temperature across the globe. *PLOS ONE* 14, e0213368. <https://doi.org/10.1371/journal.pone.0213368>.
- Qin, Y., Xiao, X., Dong, J., Zhou, Y., Zhu, Z., Zhang, G., Du, G., Jin, C., Kou, W., Wang, J., Li, X., 2015. Mapping paddy rice planting area in cold temperate climate region through analysis of time series Landsat 8 (OLI), Landsat 7 (ETM+) and MODIS imagery. *ISPRS J. Photogramm. Remote Sens.* 105, 220–233. <https://doi.org/10.1016/j.isprsjprs.2015.04.008>.
- Randerson, J.T., Liu, H., Flanner, M.G., Chambers, S.D., Jin, Y., Hess, P.G., Pfister, G., Mack, M.C., Treseder, K.K., Welp, L.R., Chapin, F.S., Harden, J.W., Goulden, M.L., Lyons, E., Neff, J.C., Schuur, E., a. G. C.S., Zender, 2006. The impact of boreal forest fire on climate warming. *Science* 314, 1130–1132. <https://doi.org/10.1126/science.1132075>.
- Roberts, S., Vertessy, R., Grayson, R., 2001. Transpiration from Eucalyptus sieberi (L. Johnson) forests of different age. *Forest Ecology and Management, Special Issue: THE SCIENCE OF MANAGING FORESTS TO SUSTAIN*. 143, pp. 153–161. [https://doi.org/10.1016/S0378-1127\(00\)00514-4](https://doi.org/10.1016/S0378-1127(00)00514-4).
- Running, S.W., Mu, Q., Zhao, M., Moreno, A., 2019. MODIS Global Terrestrial Evapotranspiration (ET) Product (MOD16A2/A3 and Year-end Gap-filled MOD16A2GF/A3GF) NASA Earth Observing System MODIS Land Algorithm (For Collection 6). National Aeronautics and Space Administration, Washington, DC, USA.
- Russell, R.E., Saab, V.A., Dudley, J.G., Rotella, J.J., 2006. Snag longevity in relation to wildfire and postfire salvage logging. *For. Ecol. Manag.* 232, 179–187. <https://doi.org/10.1016/j.foreco.2006.05.068>.
- Sall, J., Stephens, M.L., Lehman, A., Loring, S., 2017. *JMP Start Statistics: A Guide to Statistics and Data Analysis Using JMP*. Sixth edition. SAS Institute.
- Senf, C., Pflugmacher, D., Wulder, M.A., Hostert, P., 2015. Characterizing spectral-temporal patterns of defoliation and bark beetle disturbances using landsat time series. *Remote Sens. Environ.* 170, 166–177. <https://doi.org/10.1016/j.rse.2015.09.019>.
- Shen, W., Li, M., Huang, C., He, T., Tao, X., Wei, A., 2019. Local land surface temperature change induced by afforestation based on satellite observations in Guangdong plantation forests in China. *Agric. For. Meteorol.* 276–277, 107641. <https://doi.org/10.1016/j.agrformet.2019.107641>.
- Shukla, J., Nobre, C., Sellers, P., 1990. Amazon deforestation and climate change. *Science* 247, 1322–1325. <https://doi.org/10.1126/science.247.4948.1322>.
- Stuenzi, S.M., Schaepman-Strub, G., 2020. Vegetation trajectories and shortwave radiative forcing following boreal forest disturbance in Eastern Siberia. *J. Geophys. Res. Biogeosci.* 125, e2019JG005395. <https://doi.org/10.1029/2019JG005395>.
- Swann, A.L.S., Laguë, M.M., Garcia, E.S., Field, J.P., Breshers, D.D., Moore, D.J.P., Saleska, S.R., Stark, S.C., Villegas, J.C., Law, D.J., Minor, D.M., 2018. Continental-scale consequences of tree die-offs in North America: identifying where forest loss matters most. *Environ. Res. Lett.* 13, 055014. <https://doi.org/10.1088/1748-9326/aabaf0>.
- Thornton, M.M., Thornton, P.E., Wei, Y., Vose, R.S., Boyer, A.G., 2017. Daymet: Station-level Inputs and Model Predicted Values for North America, Version 3. ORNL DAAC <https://doi.org/10.3334/ORNDAAC/1391>.

- Traversa, G., Fugazza, D., Senese, A., Frezzotti, M., 2021. Landsat 8 OLI Broadband Albedo Validation in Antarctica and Greenland. *Remote Sens.* 13 (4), 799. <https://doi.org/10.3390/rs13040799>.
- van der Molen, M.K., van den Hurk, B.J.J.M., Hazeleger, W., 2011. A dampened land use change climate response towards the tropics. *Clim. Dyn.* 37, 2035–2043. <https://doi.org/10.1007/s00382-011-1018-0>.
- van der Werf, G.R., Morton, D.C., DeFries, R.S., Olivier, J.G.J., Kasibhatla, P.S., Jackson, R.B., Collatz, G.J., Randerson, J.T., 2009. CO₂ emissions from forest loss. *Nat. Geosci.* 2, 737–738. <https://doi.org/10.1038/ngeo671>.
- Vanderhoof, M.K., Williams, C.A., 2015. Persistence of MODIS evapotranspiration impacts from mountain pine beetle outbreaks in lodgepole pine forests, south-central Rocky Mountains. *Agric. For. Meteorol.* 200, 78–91. <https://doi.org/10.1016/j.agrformet.2014.09.015>.
- Vanderhoof, M., Williams, C.A., Ghimire, B., Rogan, J., 2013. Impact of mountain pine beetle outbreaks on forest albedo and radiative forcing, as derived from moderate resolution imaging spectroradiometer, Rocky Mountains, USA. *J. Geophys. Res. Biogeosci.* 118, 1461–1471. <https://doi.org/10.1002/jgrg.20120>.
- Vanderhoof, M., Williams, C.A., Shuai, Y., Jarvis, D., Kulakowski, D., Masek, J., 2014. Albedo-induced radiative forcing from mountain pine beetle outbreaks in forests, south-central Rocky Mountains: magnitude, persistence, and relation to outbreak severity. *Biogeosciences* 11, 563–575. <https://doi.org/10.5194/bg-11-563-2014>.
- Vermote, E., Justice, C., Claverie, M., Franch, B., 2016. Preliminary analysis of the performance of the Landsat 8/OLI land surface reflectance product. *Remote Sensing of Environment, Landsat 8 Science Results*. 185, pp. 46–56. <https://doi.org/10.1016/j.rse.2016.04.008>.
- Vertessy, R.A., Watson, F.G.R., O'Sullivan, S.K., 2001. Factors determining relations between stand age and catchment water balance in mountain ash forests. *Forest Ecology and Management, Special Issue: THE SCIENCE OF MANAGING FORESTS TO SUSTAIN*. 143, pp. 13–26. [https://doi.org/10.1016/S0378-1127\(00\)00501-6](https://doi.org/10.1016/S0378-1127(00)00501-6).
- Wang, G., Eltahir, E.A.B., 2000. Biosphere–atmosphere interactions over West Africa. II: multiple climate equilibria. *Q. J. R. Meteorol. Soc.* 126, 1261–1280. <https://doi.org/10.1002/qj.49712656504>.
- Wang, Z., Erb, A.M., Schaaf, C.B., Sun, Q., Liu, Y., Yang, Y., Shuai, Y., Casey, K.A., Román, M.O., 2016. Early spring post-fire snow albedo dynamics in high latitude boreal forests using Landsat-8 OLI data. *Remote Sensing of Environment Landsat 8 Science Results*. 185, pp. 71–83. <https://doi.org/10.1016/j.rse.2016.02.059>.
- LBA 55–1–LBA 55–8Werth, D., Avissar, R., 2002. The local and global effects of Amazon deforestation. *J. Geophys. Res. Atmos.* 107. <https://doi.org/10.1029/2001JD000717>.
- Wickham, J., Wade, T.G., Riitters, K.H., 2014. An isoline separating relatively warm from relatively cool wintertime forest surface temperatures for the southeastern United States. *Glob. Planet. Chang.* 120, 46–53. <https://doi.org/10.1016/j.gloplacha.2014.05.012>.
- Winckler, J., Reick, C.H., Pongratz, J., 2017. Robust identification of local biogeophysical effects of land-cover change in a global climate model. *J. Clim.* 30, 1159–1176. <https://doi.org/10.1175/JCLI-D-16-0067.1>.
- Wu, Q., Lane, C.R., Li, X., Zhao, K., Zhou, Y., Clinton, N., DeVries, B., Golden, H.E., Lang, M.W., 2019. Integrating LiDAR data and multi-temporal aerial imagery to map wetland inundation dynamics using Google earth engine. *Remote Sens. Environ.* 228, 1–13. <https://doi.org/10.1016/j.rse.2019.04.015>.
- Xu, X., Jia, G., Zhang, X., Riley, W.J., Xue, Y., 2020. Climate regime shift and forest loss amplify fire in Amazonian forests. *Glob. Chang. Biol.* 26, 5874–5885. <https://doi.org/10.1111/gcb.15279>.
- Yang, L., Jin, S., Danielson, P., Homer, C., Gass, L., Bender, S.M., Case, A., Costello, C., Dewitz, J., Fry, J., Funk, M., Granneman, B., Liknes, G.C., Rigge, M., Xian, G., 2018. A new generation of the United States National Land Cover Database: requirements, research priorities, design, and implementation strategies. *ISPRS J. Photogramm. Remote Sens.* 146, 108–123. <https://doi.org/10.1016/j.isprsjprs.2018.09.006>.
- Yuan, X., Hamdi, R., Ochege, F.U., De Maeyer, P., Kurban, A., Chen, X., 2021. Assessment of surface roughness and fractional vegetation coverage in the CoLM for modeling regional land surface temperature. *Agric. For. Meteorol.* 303, 108390. <https://doi.org/10.1016/j.agrformet.2021.108390>.
- Zhang, Y., Liang, S., 2014. Surface radiative forcing of forest disturbances over northeastern China. *Environ. Res. Lett.* 9, 024002. <https://doi.org/10.1088/1748-9326/9/2/024002>.
- Zhang, Y., Kong, D., Gan, R., Chiew, F.H.S., McVicar, T.R., Zhang, Q., Yang, Y., 2019. Coupled estimation of 500 m and 8-day resolution global evapotranspiration and gross primary production in 2002–2017. *Remote Sens. Environ.* 222, 165–182. <https://doi.org/10.1016/j.rse.2018.12.031>.
- Zhao, K., Jackson, R.B., 2014. Biophysical forcings of land-use changes from potential forestry activities in North America. *Ecol. Monogr.* 84, 329–353. <https://doi.org/10.1890/12-1705.1>.
- Zhao, K., Wulder, M.A., Hu, T., Bright, R., Wu, Q., Qin, H., Li, Y., Toman, E., Mallick, B., Zhang, X., Brown, M., 2019. Detecting change-point, trend, and seasonality in satellite time series data to track abrupt changes and nonlinear dynamics: a Bayesian ensemble algorithm. *Remote Sens. Environ.* 232, 111181. <https://doi.org/10.1016/j.rse.2019.04.034>.
- Zhou, L., Tian, Y., Baidya Roy, S., Thorncroft, C., Bosart, L.F., Hu, Y., 2012. Impacts of wind farms on land surface temperature. *Nat. Clim. Chang.* 2, 539–543. <https://doi.org/10.1038/nclimate1505>.
- Zhou, Y., Li, X., Asrar, G.R., Smith, S.J., Imhoff, M., 2018. A global record of annual urban dynamics (1992–2013) from nighttime lights. *Remote Sens. Environ.* 219, 206–220. <https://doi.org/10.1016/j.rse.2018.10.015>.